

JGR Atmospheres

RESEARCH ARTICLE

10.1029/2020JD034110

Seasonal Variation of Wet Deposition of Black Carbon at Ny-Ålesund, Svalbard



Key Points:

- Black carbon (BC) mass in air and hydrometeors at Ny-Ålesund were statistically correlated, being high in winter-spring and low in summer
- Annual BC concentrations in hydrometeors were lower by a factor of 2.8 at Ny-Ålesund than at Barrow, reflecting lower BC in air
- BC size distributions in hydrometeors were stable in the Arctic, due to size-independent wet removal during transport from lower latitudes

Supporting Information:

Supporting Information may be found in the online version of this article.

Correspondence to:

T. Mori,
mori_t@eps.s.u-tokyo.ac.jp;
mori@rs.tus.ac.jp











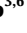


Citation:

Mori, T., Kondo, Y., Ohata, S., Goto-Azuma, K., Fukuda, K., Ogawa-Tsukagawa, Y., et al. (2021). Seasonal variation of wet deposition of black carbon at Ny-Ålesund, Svalbard. *Journal of Geophysical Research: Atmospheres*, 126, e2020JD034110. <https://doi.org/10.1029/2020JD034110>

Received 18 OCT 2020
 Accepted 18 MAY 2021

Author Contributions:

Conceptualization: Tatsuhiro Mori
Data curation: Tatsuhiro Mori, Sho Ohata, Naga Oshima, Masanori Yabuki, Wenche Aas
Formal analysis: Tatsuhiro Mori, Kaori Fukuda, Yoshimi Ogawa-Tsukagawa, P. R. Sinha
Funding acquisition: Tatsuhiro Mori, Yutaka Kondo, Sho Ohata, Kumiko Goto-Azuma, Makoto Koike, Naga Oshima, Hitoshi Matsui

Tatsuhiro Mori^{1,2} , Yutaka Kondo³ , Sho Ohata^{4,5} , Kumiko Goto-Azuma^{3,6} , Kaori Fukuda³, Yoshimi Ogawa-Tsukagawa³, Nobuhiro Moteki² , Atsushi Yoshida² , Makoto Koike² , P. R. Sinha⁷ , Naga Oshima⁸ , Hitoshi Matsui⁹ , Yutaka Tobo^{3,6} , Masanori Yabuki¹⁰ , and Wenche Aas¹¹ 

¹Department of Physics, Faculty of Science Division I, Tokyo University of Science, Tokyo, Japan, ²Department of Earth and Planetary Science, Graduate School of Science, The University of Tokyo, Tokyo, Japan, ³National Institute of Polar Research, Tachikawa, Japan, ⁴Institute for Space-Earth Environmental Research, Nagoya University, Nagoya, Japan, ⁵Institute for Advanced Research, Nagoya University, Nagoya, Japan, ⁶The Graduate University for Advanced Studies, SOKENDAI, Tachikawa, Japan, ⁷Department of Earth and Space Sciences, Indian Institute of Space Science and Technology, Thiruvananthapuram, India, ⁸Meteorological Research Institute, Tsukuba, Japan, ⁹Graduate School of Environmental Studies, Nagoya University, Nagoya, Japan, ¹⁰Research Institute for Sustainable Humanosphere, Kyoto University, Kyoto, Japan, ¹¹Norwegian Institute for Air Research, Kjeller, Norway

Abstract Black carbon (BC) aerosol deposited in and onto Arctic snow increases the snow's absorption of solar radiation and accelerates snowmelt. Concentrations of BC in the Arctic atmosphere and snow are controlled by wet deposition; however, details of this process are poorly understood owing to the scarcity of time-resolved measurements of BC in hydrometeors. We measured mass concentrations of BC in hydrometeors (C_{MBC}) and in air (M_{BC}) with 16% and 15% accuracies, respectively, at Ny-Ålesund, Svalbard during 2012–2019. Median monthly M_{BC} and C_{MBC} values showed similar seasonal variations, being high in winter-spring and low in summer. Median monthly BC wet deposition mass flux (F_{MBC}) was highest in winter and lowest in summer, associated with seasonal patterns of C_{MBC} and precipitation. Seasonally averaged BC size distributions in hydrometeors were similar except for summer. Measurements of M_{BC} and C_{MBC} in spring 2017 showed a size-independent removal efficiency, indicating that BC-containing particles were efficiently activated into cloud droplets. These observations at Ny-Ålesund were compared with observations at Barrow, Alaska, during 2013–2017. The near-surface M_{BC} at Ny-Ålesund and Barrow had similar seasonal patterns; however, the two sites differed in C_{MBC} and F_{MBC} . In summer, C_{MBC} was low at Ny-Ålesund but moderate at Barrow, likely reflecting differences in M_{BC} in the lower troposphere. Seasonally averaged BC size distributions in hydrometeors were similar at both sites, suggesting that average BC size distributions are similar in the Arctic lower troposphere. The efficiency of BC removal tends to be size-independent during transport, leading to the observed similarity.

Plain Language Summary Black carbon (BC) aerosol absorbs sunlight and heats the atmosphere. Deposition of BC in and onto Arctic snow accelerates snowmelt by reducing the snow albedo. Although wet deposition strongly controls mass concentrations of BC in air (M_{BC}) and in raindrops and snowflakes (i.e., hydrometeors; C_{MBC}), measurements of C_{MBC} are scarce. We measured C_{MBC} and M_{BC} at Ny-Ålesund, Svalbard with high accuracy during 2012–2019. The median monthly values of M_{BC} and C_{MBC} were high in winter and spring and low in summer. The size distributions of BC in air and hydrometeors were similar, suggesting that BC-containing particles are efficiently activated to become the nuclei of cloud droplets. When we compared our data to similar measurements made in Alaska during 2013–2017, we found that the two sites had different seasonal patterns of C_{MBC} and BC wet deposition flux, likely due to seasonal variations of M_{BC} in the lower troposphere. Seasonally averaged BC size distributions in hydrometeors were similar at both sites, suggesting that average BC size distributions are similar throughout the Arctic lower troposphere. We interpreted this similarity as the result of BC coating occurring at lower latitudes. Our datasets are very useful for constraining and testing climate models.

© 2021. The Authors.

This is an open access article under the terms of the [Creative Commons Attribution License](https://creativecommons.org/licenses/by/4.0/), which permits use, distribution and reproduction in any medium, provided the original work is properly cited.

Investigation: Tatsuhiko Mori, Sho Ohata, Kumiko Goto-Azuma, Nobuhiro Moteki, Atsushi Yoshida, P. R. Sinha, Yutaka Tobo
Methodology: Tatsuhiko Mori, Sho Ohata, Nobuhiro Moteki, Atsushi Yoshida
Project Administration: Yutaka Kondo, Makoto Koike
Supervision: Yutaka Kondo, Makoto Koike
Writing – original draft: Tatsuhiko Mori
Writing – review & editing: Tatsuhiko Mori, Yutaka Kondo

1. Introduction

Black carbon (BC) particles efficiently absorb solar radiation and lead to heating of the atmosphere. Moreover, BC deposited on surface snow reduces the snow albedo and accelerates snowmelt (AMAP, 2015; Bond et al., 2013; Hadley & Kirchstetter, 2012; Wang et al., 2020). Recent global climate models in the framework of the sixth phase of the Coupled Model Intercomparison Project (CMIP6; Eyring et al., 2016) have estimated that BC is the second-largest positive effective radiative forcing in the Arctic, after carbon dioxide (Oshima et al., 2020). Because radiative forcing is strongly controlled by the distribution of BC concentrations, it is critically important to estimate BC concentrations accurately in the Arctic. In general, BC particles emitted from midlatitudes and transported to the Arctic as well as those emitted in the Arctic are removed from the atmosphere mainly by wet deposition (Koike et al., 2021; Schmale et al., 2018; Willis et al., 2018). Wet deposition is a key process controlling the spatial distribution of BC in the Arctic atmosphere and snow (Huang, Gong, Jia, et al., 2010; Mahmood et al., 2016; Matsui & Moteki, 2020).

The majority of global climate models have indicated that the amount of wet deposition of BC in the Arctic region ($>66^{\circ}\text{N}$) is high in summer and low in winter, depending strongly on the spatial and temporal distribution of precipitation amount (Mahmood et al., 2016; Sharma et al., 2013). However, the magnitude and the seasonality of calculated wet deposition amounts have not been fully tested against observational data, partly because few suitable datasets (e.g., BC concentrations in snow and rain) exist to quantify wet deposition of BC in the Arctic. Therefore, it is critically important to measure BC concentrations in hydrometeors (falling snow and rain) for quantitative investigations of BC wet deposition in the Arctic.

The size distributions of BC in hydrometeors, mass concentration of BC in hydrometeors (C_{MBC}), and number concentration of BC in hydrometeors (C_{NBC}) can be measured by using a system combining a single-particle soot photometer (SP2), based on a laser-induced incandescence technique, with a concentric pneumatic nebulizer (Katich et al., 2017; Mori et al., 2016). This measurement system has been applied to hydrometeor and snowpack samples in several Arctic regions (Jacobi et al., 2019; Konya et al., 2021; Mori et al., 2019, 2020; Sinha et al., 2018). Sinha et al. (2018) used an SP2 to measure C_{MBC} in daily snowfall samples during the snowfall season (September–April) at Ny-Ålesund, Spitsbergen, in the Svalbard archipelago, to document the temporal variations of C_{MBC} and BC wet deposition flux during that period. Jacobi et al. (2019) measured C_{MBC} in snowpack at Ny-Ålesund during November–April, quantifying the amount of BC deposited in the snow column. However, the BC wet deposition flux at this site at other times of year has not been investigated in detail.

Mori et al. (2020) used an SP2 to measure C_{MBC} in daily snowfall and rainfall samples at Barrow Atmospheric Baseline Observatory near Utqiagvik in Alaska (Barrow hereafter) during 2013–2017. They showed that BC wet deposition flux by mass (F_{MBC}), derived from C_{MBC} and precipitation amount, is highest in summer because C_{MBC} and precipitation amount are both highest at that time. Calculations of C_{MBC} and F_{MBC} by two global models have suggested that the enhancement of C_{MBC} in summer arises from the increase of BC mass concentration in air (M_{BC}) in the lower free troposphere originating from biomass burning (Mori et al., 2020). However, it is not clear if these features of BC wet deposition are common in the Arctic. Further measurements of C_{MBC} and F_{MBC} at other locations with different environmental settings are required to elucidate the variations of BC wet deposition in wider regions of the Arctic.

It is well known that aerosol particles are activated as cloud condensation nuclei, depending on their microphysical properties (e.g., size and chemical composition), and incorporated into cloud droplets (Moteki et al., 2019; Motos et al., 2019; Ohata, Moteki et al., 2016; Schroder et al., 2015). In mixed-phase clouds, the Wegener-Bergeron-Findeisen (WBF) and riming processes also affect the wet deposition of BC. The WBF process leads to the efficient release of aerosol particles from droplets, which is caused by the difference between the saturation vapor pressures over ice and liquid water in mixed-phase clouds (Cozic et al., 2007; Qi et al., 2017). The riming process leads to the efficient removal of aerosol particles as a result of collisions between falling ice particles (snowflakes and ice crystals) and water droplets in clouds (Hegg et al., 2011; Macdonald et al., 2017). A numerical study with a global model has investigated the effect of the WBF process (Qi et al., 2017) by treating the degree of BC scavenging as a function of in-cloud temperature, as

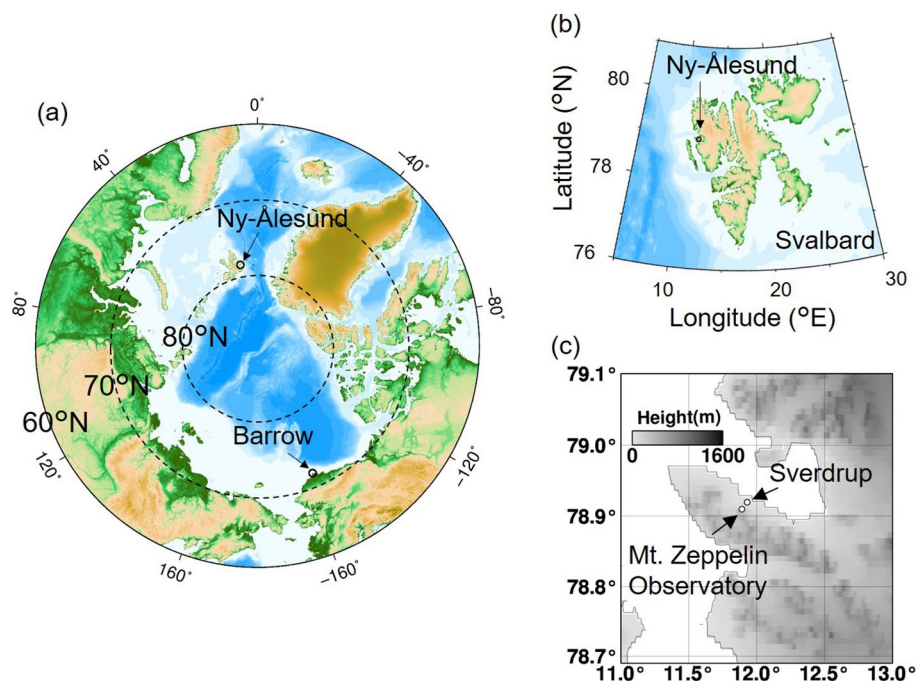


Figure 1. (a) Location map of the Northern Hemisphere ($>60^{\circ}\text{N}$) showing measurement sites at Ny-Ålesund and Barrow. (b) Map of Svalbard showing the location of Ny-Ålesund. (c) Topographic map showing observation sites near Ny-Ålesund.

measured at Jungfrauoch in Switzerland (Cozic et al., 2007). The calculations suggested that by incorporating the WBF process, M_{BC} in the free troposphere (~ 4 km altitude) increases by 45%–95%, whereas C_{MBC} and F_{MBC} decrease by $\sim 15\%$ and 22%–29%, respectively, in the Arctic (60°N – 90°N) (Qi et al., 2017). These model analyses suggest that BC wet deposition in the Arctic is affected by the WBF process in mixed-phase clouds. However, this simulated effect of the WBF process has not been fully tested with observations, mainly due to the paucity of C_{MBC} and F_{MBC} measurements.

To quantitatively understand the characteristics of BC wet deposition in the Arctic, we collected daily samples of snow and rain at Sverdrup Research Station at Ny-Ålesund (Ny-Ålesund, hereafter) from August 2012 to October 2019, and we measured C_{MBC} and C_{NBC} along with M_{BC} at Zeppelin Observatory on top of Mt. Zeppelin near Ny-Ålesund as well as meteorological parameters and cloud-base heights. In addition, BC wet deposition flux was derived from precipitation amounts and the BC concentrations in hydrometeors. We first present the temporal variations of the observed parameters (M_{BC} , C_{MBC} , F_{MBC} , precipitation, and size distributions of BC in hydrometeors) at Ny-Ålesund. We then compare these quantities with those measured at Barrow from July 2013 to August 2017 (Mori et al., 2020).

The locations of the observation sites are shown in Figure 1. Local BC emissions from anthropogenic and biomass burning sources near Ny-Ålesund and Barrow are negligible (Lamarque et al., 2010). The relevant measurements are listed in Table 1. The parameters used in this study are summarized in Table A1 of Mori et al. (2020).

2. Measurements

2.1. BC in Air

Our M_{BC} measurements were made with a continuous soot monitoring system (COSMOS; Kanomax, Inc.) at Zeppelin Observatory just south of Ny-Ålesund (78.91°N , 11.88°E , 474 m elevation), using a PM_{10} impactor inlet. This system measures the light absorption coefficient of BC particles ($<1.0 \mu\text{m}$) on a quartz-fiber filter (Pallflex E70-2075 W) with a time resolution of 1 min. The interference from light-scattering particles on the filter is negligible because these particles are removed during passage through a heated inlet (300°C).

Table 1
Measurement Parameters for Observation Sites at Ny-Ålesund

Site	Latitude (°N)	Longitude (°E)	Elevation (m)	Measurements
Zeppelin Observatory	78.91	11.88	474	BC mass concentration in ambient air
Sverdrup Research Station	78.92	11.93	5.0	Collection of snow and rain samples
Automatic Weather Station	78.92	11.93	8.0	Precipitation amount and snow depth
French-German Arctic Research (AWIPEV) Base	78.92	11.93	20	Cloud-base height
AWI Balloon Launch Site	78.92	11.92	15.5	Vertical profiles of pressure, temperature, and relative humidity

This enables M_{BC} measurements with an accuracy of about 15%, estimated by comparisons with M_{BC} simultaneously measured by the SP2 with 10% accuracy (Ohata et al., 2019). Detailed descriptions of the BC measuring system are given elsewhere (Kondo et al., 2009; Kondo, Sahu et al., 2011; Ohata et al., 2019; Sinha et al., 2017).

2.2. Collection of Snow and Rain

Daily snowfall and rainfall samples were collected at Sverdrup Research Station at Ny-Ålesund (78.92°N, 11.93°E, 5 m elevation), operated by the Norwegian Polar Institute, from August 2012 to October 2019. In total, we collected 283 snowfall samples and 273 rainfall samples (Table 2). Details of the collection techniques are described elsewhere (Mori et al., 2014, 2020; Sinha et al., 2018).

In brief, rainfall samples were collected by using a rain collector, consisting of a glass funnel and bottle, to minimize possible loss of BC particles attached to the inner wall (Mori et al., 2014, 2019). To minimize contamination during samplings, the rain collector was precleaned with pure water, routinely.

Snowfall samples were collected by using two different apparatuses (Sinha et al., 2018): a windsock was used from September 2012 to June 2016 and a box collector was used from December 2016 to October 2019. The windsock, made of plankton netting, had an opening diameter of 17 cm and a length of 40 cm. The box collector was an acrylic box (0.5 m long, 0.4 m wide, and 0.4 m high), inside of which a powder-free polyethylene bag was installed and fixed with a rubber band. Both snowfall collectors were mounted 8.5 m above the ground to avoid collecting wind-blown snow from the surface. When snow and rain were mixed, samples from the snow collector were used. Immediately after collection, the snowfall samples were melted at room temperature and then poured into precleaned vials (Sinha et al., 2018). These were kept in a refrigerator at about 5°C until transport by air freight to the University of Tokyo or the National Institute of Polar Research in Japan, where they were kept at about 5°C until analysis (Mori et al., 2020; Sinha et al., 2018).

Table 2
Seasonal and Monthly Precipitation From August 2012 to October 2019 at Ny-Ålesund

Season	Precipitation days	Sampling days ^a (snowfall, rainfall)	Monthly precipitation for all precipitation days ^b (mm month ⁻¹)	Monthly precipitation for all sampling days ^b (mm month ⁻¹)	R_j for all sampling days ^{b, c}
Winter	279	130 (124, 6)	61 (16, 87)	29 (11, 67)	0.69 (0.51, 0.83)
Spring	271	122 (114, 8)	25 (18, 43)	19 (14, 21)	0.81 (0.59, 0.89)
Summer	282	140 (25, 115)	24 (10, 51)	15 (4.2, 39)	0.79 (0.62, 0.95)
Fall	342	164 (93, 71)	53 (28, 90)	31 (10, 55)	0.84 (0.76, 0.92)

^aNumber of snow and rain samples in parentheses. ^bMedian values with 25th and 75th percentiles in parentheses. ^c R_j is defined as the ratio of the sum of daily precipitation amount for sampling events in the j th month to the total precipitation amount for all events during the j th month.

Table 3
Accuracies and Uncertainties of Parameters in This Study

Accuracy/uncertainty	Value	Explanation	References
Accuracy of M_{BC}	$\pm 15\%$	Estimate from the comparison with M_{BC} by SP2 with 10% accuracy.	Ohata et al., 2019 (Section 2.1)
Accuracy of C_{MBC} and C_{NBC}	$\pm 16\%$	Propagation of uncertainties of the pump flow rate ($\pm 5\%$), nebulizer flow rate ($\pm 5\%$), nebulizer efficiency ($\pm 10\%$), and BC concentrations in carrier gas measured by the SP2 ($\pm 10\%$).	Mori et al., 2016 (Section 2.3)
Uncertainty of C_{MBC} and C_{NBC} (rain collector)	$\pm 16\%$	Same as measurement accuracy of C_{MBC} and C_{NBC} . Negligible BC losses on the surfaces of a glass funnel and bottle during samplings.	Mori et al., 2014, 2019 (Section 2.4)
Uncertainty of C_{MBC} and C_{NBC} (box collector)	$\pm 16\%$	Same as measurement accuracy of C_{MBC} and C_{NBC} . Negligible contamination of BC particles attached to polyethylene surfaces inside the box collector and negligible BC losses on glass surfaces.	Mori et al., 2019 (Section 2.4)
Uncertainty of C_{MBC} (windsock collector)	$\pm 21\%$	Propagation of uncertainties of average mass per BC particle ($\pm 10\%$) and measurement accuracy of C_{NBC} ($\pm 16\%$).	Sinha et al., 2018 (Section 2.4)
Uncertainty of C_{NBC} (windsock collector)	$\pm 19\%$	Estimate from uncertainties of the windsock artifact correction and the C_{NBC} by comparison with the box collector	Sinha et al., 2018 (Section 2.4)
Uncertainty of precipitation amount	$\pm 30\%$ – 40%	Estimate from comparison with monthly GPCP data during 2012–2015	Mori et al., 2020 (Section 2.5)
Uncertainty of F_{MBC}	$\pm 34\%$ – 45%	Propagation of uncertainties of C_{MBC} (16%–21%) and precipitation amount (30%–40%).	Section 2.6
Uncertainty of F_{NBC}	$\pm 34\%$ – 44%	Propagation of uncertainties of C_{NBC} (16%–19%) and precipitation amount (30%–40%).	Section 2.6

2.3. BC in Snow and Rain

Mass and number size distributions of BC in hydrometeors were measured by a system consisting of a Marin-5 pneumatic nebulizer (Cetac Technologies Inc.) and the SP2 (Mori et al., 2016, 2019; 2020; Sinha et al., 2018).

The melted snow and rainwater samples were first agitated in an ultrasonic bath for 15 min to minimize the loss of BC particles attached to the glass wall (Mori et al., 2014, 2019). The water samples were injected into the nebulizer at a constant flow rate of $3.0 \times 10^{-6} \text{ L s}^{-1}$ to be aerosolized. The extraction efficiency was $50.0 \pm 4.4\%$ on average in the 70–2,000 nm size range, and it decreased linearly at larger sizes (2,000–5,000 nm). The BC and non-BC particles generated by the nebulizer were introduced into the SP2 at a flow rate of $16 \text{ cm}^3 \text{ s}^{-1}$ at standard temperature and pressure. The SP2 then measured the size-resolved BC mass and number concentrations in the carrier gas. A standard SP2 measures the mass of each BC particle with mass equivalent diameter (D_{BC}) within the 70–850 nm range by assuming a BC particle density of 1.8 g cm^{-3} (Moteki & Kondo, 2010), whereas our SP2 used in this study measures masses of BC particles within the 70–4,170 nm D_{BC} range by expanding the upper limit of the detected incandescence signal in the standard SP2 (Mori et al., 2016). Size distributions of BC in water were derived from the pump and nebulizer flow, the nebulizer efficiency, and the size distribution of BC in the carrier gas within the 70–4,170 nm D_{BC} range. We calculated C_{MBC} and C_{NBC} by integrating the mass and number size distributions, respectively, in water within the 70–4,170 nm D_{BC} range (Mori et al., 2016). This technique yields C_{MBC} and C_{NBC} measurements with an accuracy of 16% (Table 3), derived from the respective measurement uncertainties of the pump flow rate ($\pm 5\%$), nebulizer flow rate ($\pm 5\%$), nebulizer efficiency ($\pm 10\%$), and BC concentration in the carrier gas measured by the SP2 ($\pm 10\%$).

The detection of smaller BC particles strongly depends on the laser intensity in the SP2 (Schwarz et al., 2010). Laser beams with weak intensity do not completely evaporate smaller BC particles, which causes BC mass and number concentrations to be underestimated. The laser intensity of our SP2 was sufficiently strong and stable to detect BC particles with $D_{BC} = 70 \text{ nm}$ during the analysis period. In addition, our SP2 was regularly calibrated by using fullerene soot (Alpha Aeser Inc.) and maintained a similar relationship between

the masses of individual BC particles and the incandescence signals they emitted (Moteki & Kondo, 2010) during 2012–2019.

To accurately measure the size distributions of BC in hydrometeors, it is important to evaluate the stability of BC sizes during long storage periods in glass bottles. The shapes of the size distributions of BC in melted snowpack samples, collected at Ny-Ålesund, were stable and the C_{MBC} and C_{NBC} values agreed to within 20% during storage periods as long as a few years (Mori et al., 2019). Our melted snow and rain samples were analyzed within a year after their collection, thus any changes in their BC sizes were considered negligible, and the concentrations in hydrometeors were also stable during the period of storage before analysis. The size of BC particles can change by coagulation during the extraction of BC particles with a nebulizer. Mori et al. (2016) used the SP2 to measure the number size distributions of four different fullerene soot suspensions with mass concentrations ranging from 6.9 to 64 $\mu\text{g L}^{-1}$. They showed that the four distributions had similar shapes, demonstrating that the effect of coagulation during the extraction process is negligible for samples with C_{MBC} less than 64 $\mu\text{g L}^{-1}$. The annual average ($\pm 1\sigma$) value of C_{MBC} at Ny-Ålesund during 2012–2019 was $2.8 \pm 2.6 \mu\text{g L}^{-1}$, well below this upper limit.

2.4. Uncertainty in C_{MBC} Using Rain, Box, and Windsock Collectors

Table 3 summarizes the uncertainties in C_{MBC} for precipitation samples acquired by rain, box, and windsock collectors. Mori et al. (2019) showed that in our rain collector, the BC losses due to adhesion on the wall of the glass bottle are small. In addition, the glass funnel is routinely precleaned with pure water to minimize contamination during samplings. Therefore, we estimated that the additional uncertainty associated with the rain collector was negligible and the overall uncertainty in C_{MBC} was 16%.

In the case of box collectors, Sinha et al. (2018) found that contamination of BC particles attached to polyethylene surfaces inside the box collector was negligible, and by comparing C_{MBC} in snowpack and falling snow at Ny-Ålesund, they showed that dry deposition makes only a small contribution to total deposition. Considering these results, we estimated that the uncertainty introduced by snow sampling with the box collector was negligible, and thus the overall uncertainty in C_{MBC} was 16%.

The windsock collector was used to collect about 160 snowfall samples from September 2012 to June 2016, about 30% of the total number of hydrometeor samples in this study. Sinha et al. (2018) compared C_{NBC} and C_{MBC} values for 11 daily snowfall samples collected simultaneously by the windsock and box collectors at Ny-Ålesund from December 2016 to March 2017. The windsock collector samples yielded C_{NBC} and C_{MBC} values for the 70–1,000 nm D_{BC} range that on average were higher by factors of about 1.2 and 1.8, respectively, than those of the samples from the box collector. The increase is possibly due to the continued collection of ambient BC particles by the snow samples during the time they resided in the windsock; this would occur by interception and inertial impaction (Wang et al., 2010). To address this uncertainty, we first corrected the C_{NBC} values by using the cumulative C_{NBC} (integrated from 70 to 200 nm) measured in windsock samples and a correction factor of 1.1. This is a correction factor that Sinha et al. (2018) derived from the cumulative C_{NBC} value (integrated from 70 to 200 nm) of the windsock and box samples and the total C_{NBC} value (integrated from 70 nm to 4,170 nm) of the box samples for the period of December 2016–May 2017. The C_{MBC} values of these windsock samples were corrected by using the corrected C_{NBC} values and a mass per particle value of 4.67 fg, as determined by Sinha et al. (2018) from the correlation between total C_{NBC} and C_{MBC} for their snowfall samples from the box collector. The uncertainties in the corrected C_{NBC} and C_{MBC} values were 19% and 21%, respectively (Sinha et al. 2018). In this study, our analysis of BC size distributions in the snow samples relied only on data from the period when the box collector was used.

2.5. Precipitation Amount

Daily precipitation amount (P) was measured by using a Geonor weighing gauge with an Alter windshield at an automatic weather station (AWS) (78.92°N, 11.93°E, 8 m elevation), together with snow depth (Førland & Hanssen-Bauer, 2000; Hanssen-Bauer et al., 1996). The sensor accuracy of P and snow depth was about 0.1 mm and 1 cm, respectively. We classified all precipitation days as snow days or rainy days, defined as days with and without a daily increase in snow depth, respectively.

Previous studies have shown that measurement uncertainties for solid precipitation in the Arctic are caused by wind-induced undercatch, wetting, evaporation, and blowing snow (Førland & Hanssen-Bauer, 2000, 2003; Rasmussen et al., 2012). They reported that the uncertainty of P was 20%–50% when compared with total precipitation values measured by a precipitation gauge with a double fence. Considering these results, we estimated the uncertainty of monthly P values obtained from the AWS by comparing them with Global Precipitation Climatology Project (GPCP) One-Degree Daily data (<https://psl.noaa.gov/>) for the grid box including Ny-Ålesund (78°N–79°N, 11°E–12°E) based on satellite and rain gauge measurements during 2012–2015. The monthly AWS precipitation data were strongly correlated with the GPCP data during the cold season (October–May) ($r^2 = 0.84$ and AWS/GPCP = 0.62) and the warm season (June–September) ($r^2 = 0.90$ and AWS/GPCP = 0.71). Thus, the measurement uncertainties of P were about 40% during the cold season and 30% during the warm season, when compared with GPCP data, a result consistent with previous studies (Mori et al., 2020; Sinha et al., 2018). The possible bias in the AWS data was not corrected in this study.

2.6. BC Wet Deposition Flux

Detailed methods for deriving the monthly BC wet deposition flux have been described elsewhere (Mori et al., 2014, 2020). In brief, daily wet deposition flux of BC by mass (F_{MBC}) ($\mu\text{g m}^{-2} \text{d}^{-1}$) was calculated as

$$F_{MBC} = C_{MBC} \times P, \quad (1)$$

where C_{MBC} ($\mu\text{g L}^{-1}$) is daily BC mass concentration in hydrometeors and P (mm d^{-1}) is daily precipitation amount. Then, the monthly P collection rate in the j th month (R_j) was calculated, defined as the ratio of the sum of daily P for sampling events in the j th month to the total P for all events during the j th month. The monthly F_{MBC} ($\mu\text{g m}^{-2} \text{month}^{-1}$) in the j th month was derived by dividing the sum of daily F_{MBC} in the j th month by R_j . Monthly wet deposition flux of BC by number (F_{NBC}) in the j th month was similarly derived. The monthly mean C_{MBC} and C_{NBC} in the j th month were derived as the ratios $(F_{MBC})_j/P_j$ and $(F_{NBC})_j/P_j$, which represent the P -weighted C_{MBC} and C_{NBC} averages, respectively.

The seasonal median values of R_j ranged from 0.69 to 0.81, as summarized in Table 2. These were much higher than R_j values at Barrow (0.17–0.57; shown in Mori et al., 2020), indicating that our datasets of monthly F_{MBC} and F_{NBC} are statistically more reliable throughout the year because we sampled more of the month's precipitation.

Uncertainty in the estimate of the corrected C_{MBC} for windsock samples was 21% for snowfall events during 2012–2016 (Section 2.4). Except for this period, the measurement uncertainty of C_{MBC} for samples from the rain and box collectors was 16% (Section 2.3). The estimated uncertainty of monthly P values ranged from 30% to 40%, based on the comparison between AWS and GPCP data (Section 2.5). Considering these results, the uncertainty in our estimates of monthly F_{MBC} ranged from 34% to 45%. These uncertainties are summarized in Table 3.

3. Meteorology

Vertical profiles of meteorological parameters (e.g., pressure, temperature, and relative humidity) have been routinely measured near the hydrometeor sampling site by using radiosondes launched from the balloon launching site (78.92°N, 11.92°E, 15.5 m elevation) at 0000 and 1200 UTC. We used these profiles to calculate the vertical profile of water vapor mixing ratio on the basis of the Clausius-Clapeyron equation (Bolton, 1980; Murphy & Koop, 2005) and to calculate total precipitable water (TPW), representing the total amount of water vapor in a column of air.

Cloud-base heights have been continuously measured at the French-German Arctic Research (AWIPEV) Base (78.92°N, 11.93°E, 20 m elevation) by using a micropulse lidar with a Nd:YLF laser at a wavelength of 523 nm (Campbell & Shiobara, 2008; Shiobara et al., 2003), determined by using a lidar cloud detection algorithm (e.g., Campbell et al., 1998, 2002). The time resolution of the cloud-base height data is 3 min.

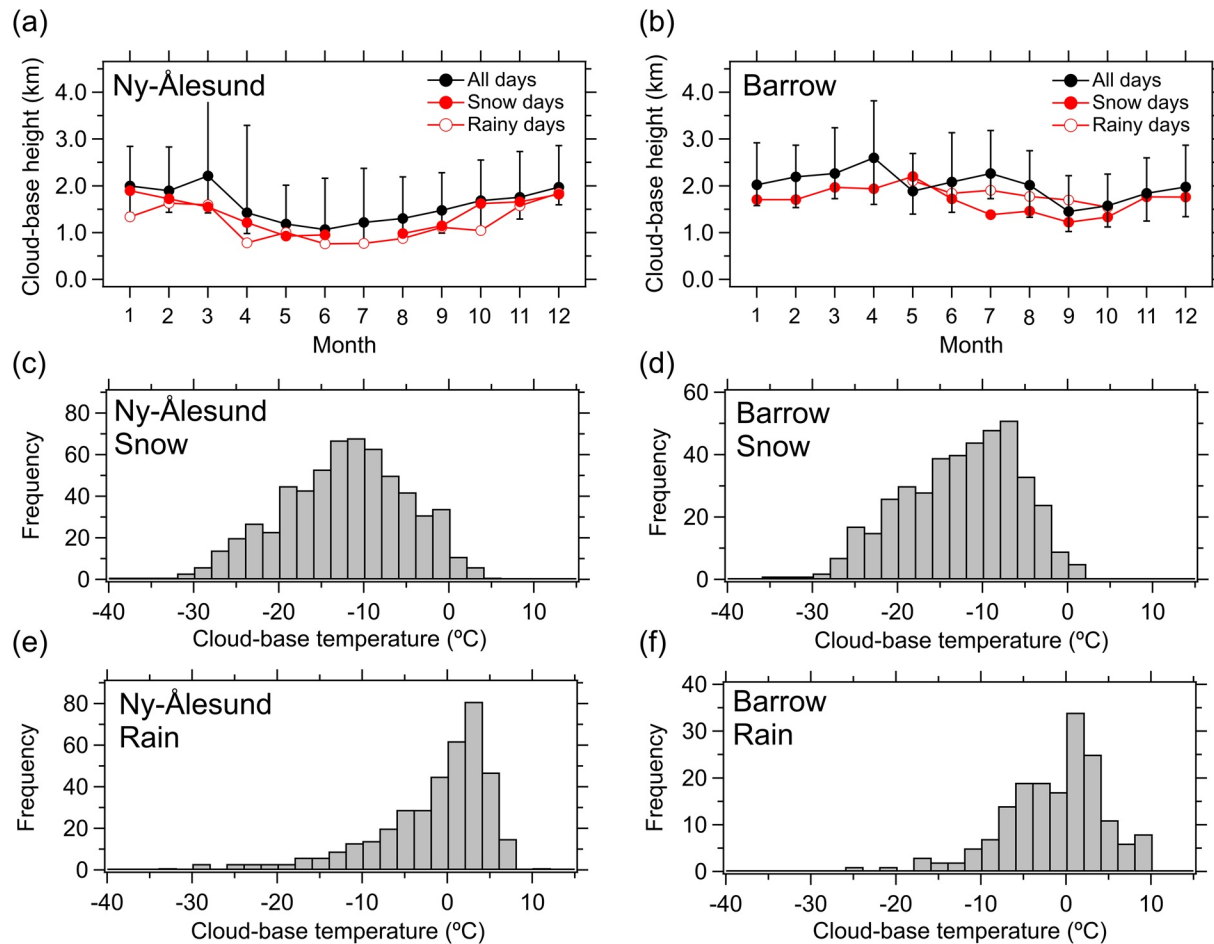


Figure 2. Median values of daily average cloud-base height for all days, snow days, and rainy days at (a) Ny-Ålesund during 2012–2019 (this study) and (b) Barrow during 2013–2017 (Mori et al., 2020), and distributions of daily average cloud-base temperature for snow days at (c) Ny-Ålesund during 2012–2019 and (d) Barrow during 2013–2017 and for rainy days at (e) Ny-Ålesund and (f) Barrow. Error bars indicate 25th and 75th percentiles for all days.

3.1. Seasonal Variations of Temperature

Monthly mean temperatures ($\pm 1\sigma$) at the altitude of Zeppelin Observatory (~ 0.5 km) during 2012–2019 had clear seasonal variations, being highest in July ($3.7 \pm 2.9^\circ\text{C}$) and lowest in March ($-11 \pm 5.8^\circ\text{C}$) (not shown). Monthly mean temperatures at higher altitudes (about 2.0 km, 3.0 km, and 4.0 km) had similar seasonal patterns. Except for the four months from June to September, monthly mean temperatures above 0.5 km were always below 0°C .

3.2. Cloud-Base Height

The micropulse lidar monitors the backscattering signal returned from optically thin and thick clouds, and the cloud-base height is determined as the altitude of the first level at which the backscattering signal sharply increases (Shiobara et al., 2003). We used the data of the cloud-base height for all optically thin and thick clouds from August 2012 to October 2019.

Median values of daily average cloud-base height displayed a clear seasonal variation (Figure 2a), being lowest in summer (1.2 km) and highest in winter (2.0 km). This pattern applied to all days in our analysis period, to the snow days and rainy days (Figure 2a), and to our sampling days (not shown).

The radiosonde measurements at Ny-Ålesund during 2012–2019 showed that average relative humidity over ice for snow and rainy days was about 90%–100% within the 0.6–1.4 km altitude range, although relative

humidity over liquid was somewhat lower. The amount of water vapor below 2.0 and 4.0 km accounted for about 70% and 90% of the TPW, respectively. In addition, the water vapor concentration below 2 km was higher on precipitation days than on nonprecipitation days. These results are consistent with the cloud-base height of 1–2 km on precipitation days.

Previous studies have investigated the features of cloud-base height at Ny-Ålesund by using micropulse lidar and ceilometer measurements. One of the studies found that the cloud-base height was mostly below 2 km in summer and early fall in 1998–1999 (Shiobara et al., 2003), and another reported that about 50%–75% of clouds appeared below 2 km in 2004–2013 (Yeo et al., 2018). A 25-year (1992–2017) data set of ceilometer measurements showed that seasonally averaged cloud-base height was lowest during summer (Maturilli & Ebell, 2018). Our results are in agreement with these previous results.

To investigate the occurrence of mixed-phase clouds at Ny-Ålesund during our observation period, we compared the cloud-base heights and cloud-base temperatures with those previously measured at Barrow (Mori et al., 2020), where mixed-phase clouds are common (Shupe, 2011). By estimating cloud-base temperature from radiosonde and micropulse lidar measurements, we found that the median (25th percentile, 75th percentile) values of cloud-base temperatures at Ny-Ålesund were -12°C (-18°C , -7.4°C) on snow days and 0.4°C (-5.1°C , 2.9°C) on rainy days, and these two categories had different temperature distributions (Figures 2c and 2e). Shupe (2011) combined micropulse lidar, millimeter cloud radar, microwave radiometer, and radiosonde observations at Barrow during 2004–2006 to show that mixed-phase clouds formed mainly at 0–3 km altitude except in summer, when they formed at 2–6 km, and that temperatures in the mixed-phase clouds ranged from -14°C to 2°C . We estimated that median (25th percentile, 75th percentile) values of cloud-base temperature at Barrow during 2013–2017 were -12°C (-17°C , -6.7°C) on snow days and -0.3°C (-6.0°C , 2.8°C) on rainy days (Figures 2d and 2f). Although the cloud-base height was somewhat lower at Ny-Ålesund than at Barrow (Figures 2a and 2b), the median values and dispersions of temperature distributions were very similar at the two sites for each snow and rainy day (Figures 2c–2f). These meteorological similarities suggest that mixed-phase clouds were also common at Ny-Ålesund.

Global model calculations showed that at Barrow, about 50% of annual BC wet deposition occurred by scavenging of BC at altitudes below 1 km and about 90% occurred by scavenging of BC at altitudes below 4 km (Mori et al., 2020), which suggests that a portion of hydrometeors including BC particles originated in or passed through mixed-phase clouds at Barrow. Considering the meteorological similarities of Ny-Ålesund and Barrow, it is likely that some portion of hydrometeors at Ny-Ålesund interacted with ice particles.

Previous studies have shown that mixed-phase clouds occur mainly below 2 km at Ny-Ålesund throughout the year by combining ceilometer, cloud radar, microwave radiometer, and radiosonde measurements during 2016–2018 (Gierens et al., 2020; Nomokonova et al., 2019). These results confirm that mixed-phase clouds commonly occurred below the lower altitude (~ 2 km) during our observation periods.

4. BC Wet Removal

Time series of daily average M_{BC} and C_{MBC} at Ny-Ålesund are shown in Figure 3, and the respective monthly averages are shown in Figure 4. The monthly average M_{BC} values for precipitation days (Figure 4) were about 20% lower than those for all days ($r^2 = 0.89$) on average, which may partly be due to BC loss by precipitation. In this study, we used daily and monthly M_{BC} values for precipitation days for comparison with C_{MBC} .

In this section, we present the features of five parameters measured at Ny-Ålesund: M_{BC} , C_{MBC} , P , F_{MBC} , and size distribution in hydrometeors. Monthly averages of M_{BC} and P -weighted C_{MBC} and monthly sums of total P and F_{MBC} values were obtained for the same month during about 7 years of 2012–2019 (Table S1). For the statistical analyses of each parameter described below, we represented each month of the year by the median of about these seven monthly values, which we denote here as the median monthly value. The seasonal patterns of M_{BC} , C_{MBC} , P , and F_{MBC} at Ny-Ålesund are derived from these median monthly values, consisting of 12 data points for each parameter, to minimize the influence of extreme values. In fact, there were large variabilities (1σ) in seasonal and annual average values of these parameters at Ny-Ålesund (Table 4).

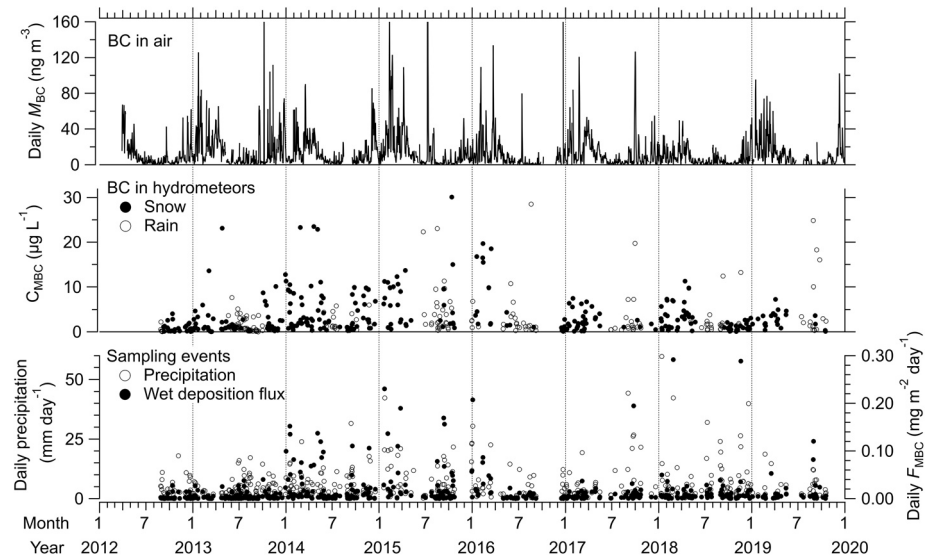


Figure 3. (upper and middle) Daily average values of M_{BC} (BC in air) and C_{MBC} (BC in snow and rain) and (lower) daily values of precipitation amount and F_{MBC} (wet deposition flux) for each sample from August 2012 to October 2019.

4.1. BC Mass Concentration in Air

Median monthly M_{BC} for precipitation days at Ny-Ålesund displayed a marked seasonal variation, being highest in spring and lowest in summer (Figure 5a and Table 4). In general, the Arctic front during winter and spring expands southward over northern Eurasia, such that air masses significantly influenced by anthropogenic BC emissions, mainly at midlatitudes, are frequently transported to the Arctic. At the same time, the strong temperature inversion causes high aerosol concentrations to accumulate in the planetary boundary layer (PBL). As a result, M_{BC} increases in winter and spring (AMAP, 2015; Browse et al., 2012; Hirdman et al., 2010; Quinn et al., 2007; Sharma et al., 2013). During summer, the Arctic front retreats far to the north, such that air masses are transported mainly from the Arctic Ocean (Eleftheriadis et al., 2009; Hirdman et al., 2010). In addition, because BC wet deposition generally increases during its long-range

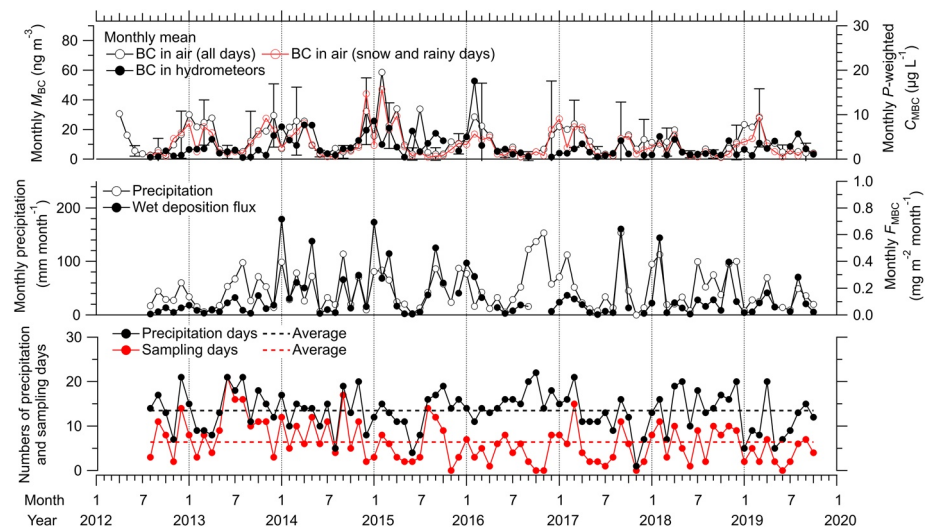


Figure 4. (top) Monthly average values of M_{BC} (black carbon [BC] in air) on all days, M_{BC} on all days with snow or rain, and P -weighted C_{MBC} (BC in hydrometeors, or snow and rain), (middle) monthly precipitation amount and F_{MBC} , and (bottom) numbers of precipitation and sampling days plus their monthly averages (13.5 and 6.4, respectively) from August 2012 to October 2019. Error bars represent uncertainties ($\pm 1\sigma$) of monthly M_{BC} for each third month.

Table 4

Seasonal and Annual Median and Average Values of Monthly Parameters at Ny-Ålesund From August 2012 to October 2019

Season		M_{BC} (ng m ⁻³)	P -weighted C_{MBC} (μg L ⁻¹)	P -weighted C_{NBC} (μ L ⁻¹)	P (mm month ⁻¹)	F_{MBC} (μg m ⁻² month ⁻¹)	F_{NBC} (10 ⁹ m ⁻² month ⁻¹)
Winter	Median	12 (9.3, 20)	2.2 (1.0, 5.1)	462 (214, 1,131)	61 (16, 87)	96 (54, 275)	24 (12, 61)
	Average	16 ± 11	3.8 ± 4.0	814 ± 871	57 ± 37	192 ± 220	44 ± 53
Spring	Median	15 (8.2, 22)	2.9 (1.7, 4.1)	583 (364, 969)	25 (18, 43)	73 (37, 140)	16 (7.3, 32)
	Average	15 ± 8.2	3.3 ± 2.1	724 ± 496	32 ± 22	125 ± 145	28 ± 35
Summer	Median	2.4 (1.8, 4.0)	1.3 (1.0, 1.9)	272 (164, 410)	24 (10, 51)	28 (12, 76)	5.8 (2.2, 14)
	Average	3.0 ± 1.6	1.9 ± 1.6	385 ± 376	33 ± 29	56 ± 67	13 ± 18
Fall	Median	5.0 (2.7, 9.5)	1.9 (0.9, 3.3)	438 (166, 823)	53 (28, 90)	69 (41, 253)	20 (5.8, 60)
	Average	7.2 ± 6.4	2.2 ± 1.6	540 ± 476	65 ± 45	162 ± 182	42 ± 52
Year	Median	6.6 (3.2, 14)	1.9 (1.1, 4.1)	415 (193, 932)	34 (18, 71)	65 (25, 148)	14 (4.8, 32)
	Average	10 ± 9.3	2.8 ± 2.6	616 ± 603	47 ± 37	133 ± 169	31 ± 43

Note. Median values are accompanied by 25th and 75th percentile values in parentheses; average values include ±1σ. Monthly C_{MBC} and C_{NBC} are P -weighted values.

transport from lower latitudes and within the Arctic, M_{BC} decreases in summer (AMAP, 2015; Browse et al., 2012; Hirdman et al., 2010; Quinn et al., 2007; Sharma et al., 2013).

A study of 20-day back trajectories from the altitude of Zeppelin Observatory (474 m) during 2002–2007, using the Lagrangian particle dispersion model FLEXPART, suggested frequent transport of polluted air masses from northern Eurasia during winter and cleaner air masses from the northern Arctic during summer (Hirdman et al., 2010). In addition, the radiosonde measurements showed that the median monthly upper boundaries of the PBL were higher in summer (~1,600 m) and lower in winter (~640 m), suggesting that Zeppelin Observatory was within the PBL throughout the year, on average.

4.2. BC Mass and Number Concentration in Hydrometeors

Median monthly P -weighted C_{MBC} and C_{NBC} at Ny-Ålesund displayed a seasonal variation like that of M_{BC} , being high in spring and low in summer (Figures 5b and S1a, Table 4). The median monthly values of P -weighted C_{MBC} and M_{BC} for all precipitation days during the observation period (Figures 5a and 5b, respectively) were well correlated ($r^2 = 0.78$; Figure 6a). In addition, the median daily values of C_{MBC} and M_{BC} were also well correlated ($r^2 = 0.44$; Figure 6b) for sampling days in which P exceeded 1.1 mm, or about 80% of all sampling days. However, monthly P -weighted average C_{MBC} was poorly correlated with monthly average M_{BC} for all seasons ($r^2 = 0.06$; not shown) and for each of the three months of winter ($r^2 = 0.01$), summer ($r^2 = 0.01$), and fall ($r^2 = 0.05$), and moderately correlated for the three months of spring ($r^2 = 0.16$) (Figure S2). The correlation between daily C_{MBC} and daily M_{BC} on sampling days was also poor (not shown).

These results indicate that the C_{MBC} – M_{BC} correlation is influenced by the variations of M_{BC} and C_{MBC} through multiple effects and processes that tend to weaken the link between the two quantities on a daily basis. First, precipitation is generally associated with physical processes, including cloud and precipitating particle formation, in volumes of air much larger than the vertical column above the measurement site. Therefore, C_{MBC} during precipitation events may not be directly linked with M_{BC} in the local air column, unless BC is uniformly distributed in the atmosphere. Second, increasing the number fraction of cloud droplets nucleated on BC-free particles leads to a decrease in C_{MBC} , considering that coalescence is a key process to grow cloud droplets to rain droplet size.

Change of M_{BC} with altitude is another factor related to the C_{MBC} – M_{BC} correlation. Some observations of the vertical profiles of BC and aerosol have been reported. Aircraft measurements of M_{BC} conducted in March 2013 at locations within ±0.5° latitude and ±3.0° longitude from Zeppelin Observatory showed that M_{BC} was rather uniform from 0.2 to 2.0 km altitude, on average (Liu et al., 2015). The Polar Airborne Measurements and Arctic Regional Climate Model Simulation Project (PAMARCMiP) campaign,

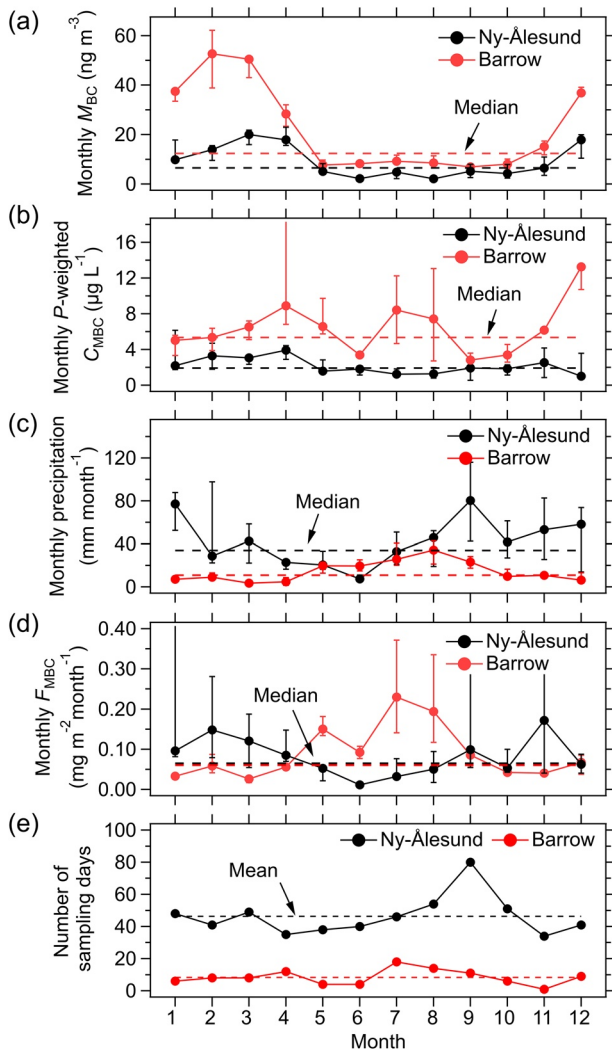


Figure 5. Seasonal variations of median monthly values of (a) M_{BC} at Ny-Ålesund during 2012–2019 (black) and at Barrow during 2013–2017 (red) plus both annual median values (dashed lines at 6.6 ng m^{-3} and 12 ng m^{-3} , respectively), (b) P -weighted C_{MBC} plus both annual median values ($1.9 \mu\text{g L}^{-1}$ and $5.4 \mu\text{g L}^{-1}$, respectively), (c) total P plus both annual median values (34 mm month^{-1} and 11 mm month^{-1} , respectively), and (d) F_{MBC} plus both annual median values ($65 \mu\text{g m}^{-2} \text{month}^{-1}$ and $62 \mu\text{g m}^{-2} \text{month}^{-1}$, respectively). (e) Number of sampling days during the observation periods plus annual mean values (46 at Ny-Ålesund and 8.4 at Barrow). Error bars indicate 25th and 75th percentiles.

only moderate ($r^2 = 0.14$). The error bars in Figure 7a indicate measurement uncertainties of 40% for median monthly P , which are not large enough to strongly influence the seasonal pattern of monthly P .

The value of P may be more strongly influenced than TPW by variabilities in synoptic disturbance through complicated dynamic and thermodynamic processes at Ny-Ålesund, weakening the correlation between P and TPW. On the other hand, the seasonal patterns of monthly TPW and P were similar at Barrow (Figure 7b), indicating that monthly P was strongly influenced by the local TPW (Mori et al., 2020). Previous studies used global models to investigate the distribution of P around Svalbard in winter (Maturilli & Kayser, 2017; Rinke et al., 2017) and in summer (Serreze & Barrett, 2008; X. D. Zhang et al., 2004). During winter, intense cyclones in the North Atlantic storm tracks lead to strong inflow of warm and moist air from

conducted over the northern polar and North Pacific regions in spring 2018, also showed that M_{BC} was vertically rather uniform from altitudes of 0.1–2.5 km (Yoshida et al., 2020). These results suggest that the rather uniform M_{BC} over Ny-Ålesund may account for the moderate correlation between monthly C_{MBC} and M_{BC} during spring. Because no observations of M_{BC} distribution near Ny-Ålesund have been made in other seasons, it is difficult to interpret the seasonal variations in the correlation between C_{MBC} and M_{BC} . Ground-based measurements near Ny-Ålesund during 2014–2017 showed that the backscattering coefficient of aerosols was vertically uniform in the PBL and lower troposphere in all seasons (Shibata et al., 2018). However, this feature may not apply to BC, and the effect of variability of vertical profiles of BC is inconclusive.

The micropulse lidar and radiosonde observations showed that a portion of the hydrometeors including BC particles may have originated in or passed through mixed-phase clouds at Ny-Ålesund (Section 3.2). Global model calculations predict that BC particles are released efficiently from cloud droplets in Arctic mixed-phase clouds due to the WBF process, likely leading to reduced BC removal (Qi et al., 2017; Shen et al., 2017). Considering this, measured C_{MBC} may be affected by the BC scavenging process in mixed-phase clouds mainly during winter and spring, when the WBF process can be important. This process may also contribute to weakening the C_{MBC} – M_{BC} correlation.

On a monthly basis, the variations of M_{BC} and C_{MBC} caused by these multiple processes may average out to some extent. However, these effects likely still degrade the C_{MBC} – M_{BC} correlation for the average ($\pm 1\sigma$) number of monthly sampling days of 6.4 ± 4.5 (Figures 4 and S2). The number of sampling days during 2012–2019 ranged within $N = 34$ –80 per calendar month (Figure 5e and Table S1). When the median values are determined by data from months with $N \approx 40$, C_{MBC} and M_{BC} are well correlated. On this statistical basis, the BC mass deposited per unit of precipitated water increases with increasing M_{BC} .

4.3. Precipitation Amount

Figure 3 shows daily P for each sampling day, and Figure 4 shows monthly P for all precipitation days at Ny-Ålesund during 2012–2019. Median monthly P for 2012–2019 showed a clear seasonal variation, decreasing from winter-spring to early summer and increasing from summer to winter (Figure 5c and Table 4).

We used TPW to investigate the effect of water vapor amount on the local P . The median monthly TPW showed a clear seasonal pattern, highest in summer and lowest in winter, but its pattern differed from that of monthly P (Figure 7a), and the correlation between monthly TPW and P was

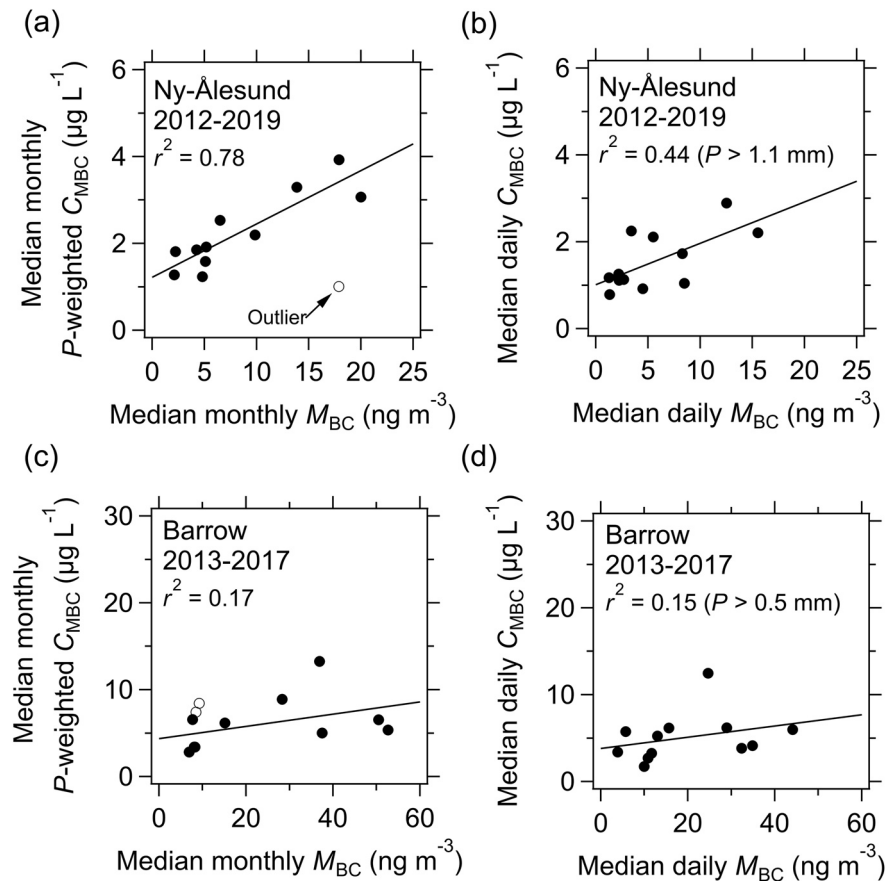


Figure 6. (a) Correlations between median monthly values of black carbon (BC) mass concentration in ambient air (M_{BC}) for all precipitation days and those of BC mass concentration in hydrometeors (C_{MBC}) at Ny-Ålesund during 2012–2019. (b) Same as (a) but for median daily values on all sampling days with precipitation amount (P) > 1.1 mm. (c) Same as (a) but for Barrow during 2013–2017. (d) Same as (b) but for Barrow on all sampling days with $P > 0.5$ mm. The regression lines were determined by the least squares method for the data at Ny-Ålesund except the extreme values of M_{BC} in December and for the data at Barrow except for July and August, when the C_{MBC} was strongly influenced by biomass burning (open symbols).

lower latitudes to the Arctic (Maturilli & Kayser, 2017; Rinke et al., 2017). Consistently, the spatial distribution of monthly P from GPCP data during winter shows a marked latitudinal gradient of P southwest of Svalbard (Figure 8a). During summer, lows over the Eurasian continent and cyclogenesis over the Arctic Ocean cause an increase in cyclonic activity over the Arctic Ocean (Serreze & Barrett, 2008; X. D. Zhang et al., 2004). In fact, values of monthly P over the Arctic Ocean are uniformly higher in summer than in winter although the precipitation amount around Ny-Ålesund is lower (Figure 8b).

4.4. BC Wet Deposition Flux

Figure 3 shows daily F_{MBC} for each sample, and Figure 4 shows the monthly F_{MBC} for all precipitation days at Ny-Ålesund during 2012–2019. Median monthly F_{MBC} and F_{NBC} displayed marked seasonal variations, being highest in winter and lowest in summer (Figures 5d and S1c, Table 4). The high F_{MBC} in winter was due to high C_{MBC} and P values, and the low F_{MBC} in summer was due to low C_{MBC} and P values.

Figure S3 shows the correlation between monthly F_{MBC} and P for each season. The monthly F_{MBC} values were strongly variable at the higher monthly P values in all seasons due to the large variability in the monthly P -weighted C_{MBC} . We characterized the variance of the monthly F_{MBC} by using the average and 1σ of monthly P -weighted C_{MBC} and P , described in detail in the Appendix. The variance of monthly F_{MBC} was associated with the variances of monthly P -weighted C_{MBC} and monthly P to comparable degrees.

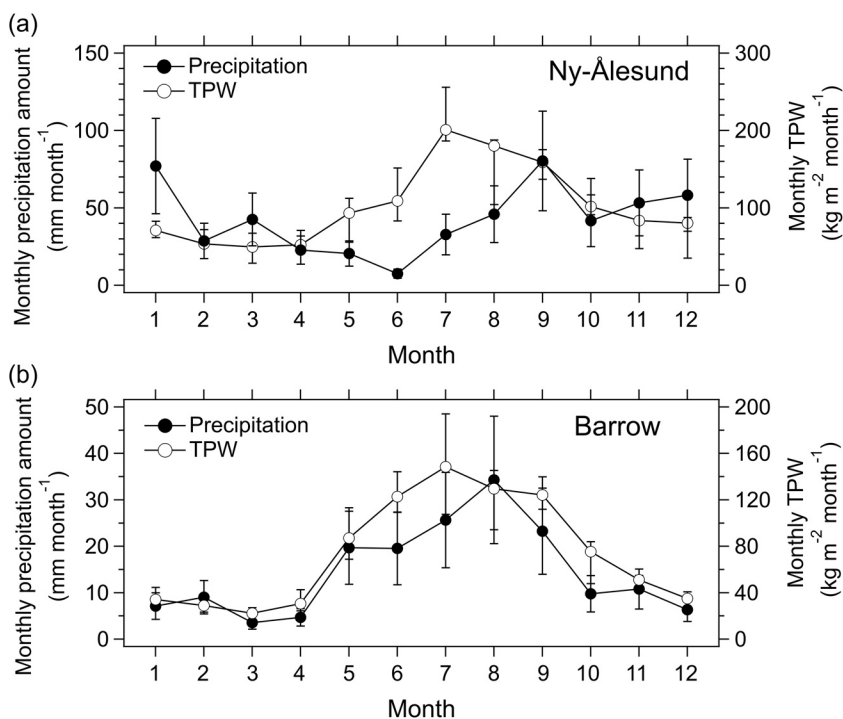


Figure 7. Median monthly precipitation amount and total precipitable water (TPW) at (a) Ny-Ålesund during 2012–2019 and at (b) Barrow during 2013–2017 (Mori et al., 2020). Error bars indicate the measurement uncertainty ($\pm 40\%$) for the monthly precipitation amount and 25th and 75th percentiles for monthly TPW.

Our estimates showed that the amount of local BC wet deposition per unit area during 2012–2019 averaged 1.60 mg m^{-2} per year, approximately 35% of which (0.58 mg m^{-2}) occurred in the 3 months of winter, for a seasonally averaged F_{MBC} value of $0.19 \text{ mg m}^{-2} \text{ month}^{-1}$. Compared to the seasonally averaged emission flux of BC from anthropogenic sources north of 55°N during 2013–2016 estimated by Mori et al. (2020), our estimate was much higher than their estimate for the latitude band $65 \pm 2.5^\circ\text{N}$ ($0.07 \text{ mg m}^{-2} \text{ month}^{-1}$) and somewhat lower than their estimate for the latitude band $60^\circ\text{N} \pm 2.5^\circ\text{N}$ ($0.29 \text{ mg m}^{-2} \text{ month}^{-1}$). These results underscore the importance of wet removal at Ny-Ålesund during winter, which was as high as the estimate of BC emission flux around 60°N .

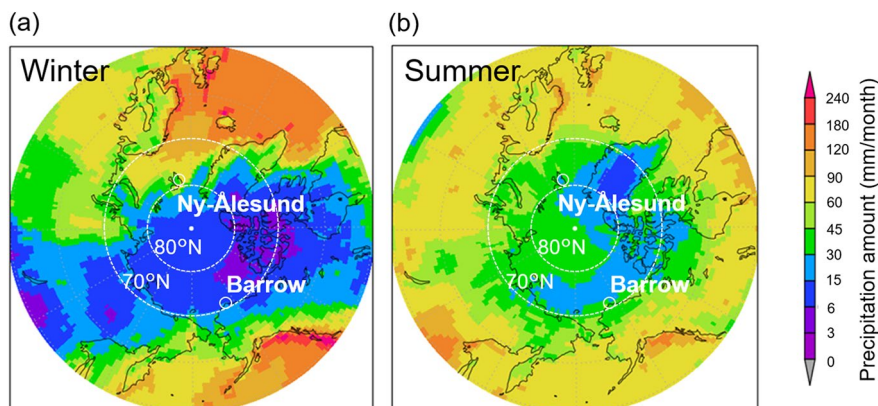


Figure 8. Spatial distribution of average precipitation for (a) winter (December–February) and (b) summer (June–August) during 2012–2019, obtained from the Global Precipitation Climatology Project Climate Data Record daily data set at a horizontal resolution of 1.0° latitude/longitude. The locations of Ny-Ålesund and Barrow are shown by white circles.

Macdonald et al. (2017) collected 17 snowfall samples at Alert in Canada during the winter of 2014–2015 and measured C_{MBC} within the 60–380 nm D_{BC} range by using a nebulizer-SP2 technique similar to ours. Their median values of daily C_{MBC} and F_{MBC} were $2.3 \mu\text{g L}^{-1}$ and $0.42 \mu\text{g m}^{-2} \text{d}^{-1}$, respectively. We collected 15 snowfall samples at Ny-Ålesund during the same period. The median value of daily F_{MBC} at Ny-Ålesund ($20 \mu\text{g m}^{-2} \text{d}^{-1}$) was much higher than at Alert, a result of higher median values of daily C_{MBC} ($6.3 \mu\text{g L}^{-1}$) and P (4.6mm d^{-1}). The average ($\pm 1\sigma$) ratio of C_{MBC} ($D_{\text{BC}} = 70\text{--}380 \text{ nm}$) to total C_{MBC} ($D_{\text{BC}} = 70\text{--}4,170 \text{ nm}$) was 0.62 ± 0.19 at Ny-Ålesund, indicating that differences in the BC size range measured were not the major cause of the large difference in F_{MBC} between Ny-Ålesund and Alert.

4.5. Size Distributions of BC

4.5.1. Snow and Rain

BC in hydrometeors had similar mass size distributions in all seasons except summer, when the size distribution shifted toward smaller sizes (Figure 9c), whereas their number size distributions were similar throughout the year (Figure 9d). In addition, hydrometeors on snow and rainy days had similar seasonally averaged BC mass size distributions in all seasons except winter, when only a few samples were collected on rainy days (Figures 9e–9h). The number size distributions on snow and rainy days were also similar (not shown). Note that the annual mass and number size distributions of BC in hydrometeors (Figures 9a and 9b, respectively) had large variabilities, represented by error bars (25th and 75th percentiles) for each size category.

We quantified the features of the BC size distributions with the following parameters: mass median diameter (MMD), count median diameter (CMD), geometric standard deviations (σ_{gm} and σ_{gc}) for the mass and number size distributions in precipitation, the ratio of C_{MBC} for larger particles ($D_{\text{BC}} = 600\text{--}4,170 \text{ nm}$) to total C_{MBC} ($D_{\text{BC}} = 70\text{--}4,170 \text{ nm}$), or f_{600} , and BC mass per particle m_{BC} ($\equiv C_{\text{MBC}}/C_{\text{NBC}}$), as summarized in Table 5. The f_{600} and m_{BC} parameters are useful for investigating changes in the size distribution of BC particles, and they were well correlated with each other ($r^2 = 0.49$). The choice of 600 nm is somewhat arbitrary, and other diameters can be used as thresholds, for example, 800 nm (f_{800}) and 1,000 nm (f_{1000}). The ratios f_{800} and f_{1000} were strongly correlated with f_{600} ($r^2 = 0.93$ and 0.88 , respectively), consistent with the result of Mori et al. (2019). The median values of f_{600} and m_{BC} on the sampling days were somewhat larger in winter than in summer, corresponding to the differences in the shapes of the size distributions in the two seasons (Table 5 and Figure 9).

The ratio of C_{NBC} for smaller particles ($D_{\text{BC}} = 10\text{--}70 \text{ nm}$) to total C_{NBC} ($D_{\text{BC}} = 10\text{--}4,170 \text{ nm}$) was estimated to be about 0.30 (Figure S4). The mass contribution of the smaller particles to the total C_{MBC} was negligible (Figure 9a).

4.5.2. Snow and Air

We investigated the size dependence of BC wet deposition by comparing the number size distributions of BC in hydrometeors and BC in ambient air. We measured the BC number and mass size distributions in air and the mixing states of BC-containing particles at Zeppelin Observatory from February 28 to 4 March 4, 2017 and from March 21 to 29, 2017, using our standard SP2 (Ohata et al., 2019). These campaign data consisted of 1-h averages within the 70–850 nm D_{BC} range and 1-h average mixing states of BC-containing particles with D_{BC} of $\sim 186 \text{ nm}$. As an indicator of the mixing state, we used the mass-equivalent shell-to-core ratio, defined as the ratio of the diameter of a BC-containing particle with $D_{\text{BC}} = 186 \text{ nm}$ to that of the BC-core particle. A detailed description of the method to derive the shell-to-core ratio is given in Moteki et al. (2019).

Table S2 shows average values related to BC in air during the whole campaign period and those in snow samples collected at Sverdrup Research Station on three different days during the campaign period (March 4, 23, and 24, 2017). The average shape of the BC size distributions from the three precipitation days was very similar to the size distribution for the whole campaign period (Figure S5). The median values of M_{BC} , MMD, and shell-to-core ratio were also comparable to those measured by Zanatta et al. (2018) at the same site in spring of 2012. In addition, the average values of CMD, σ_{gc} , and σ_{gm} in hydrometeors during the campaign period were also comparable to the annual median values of those parameters in March of 2012–2019,

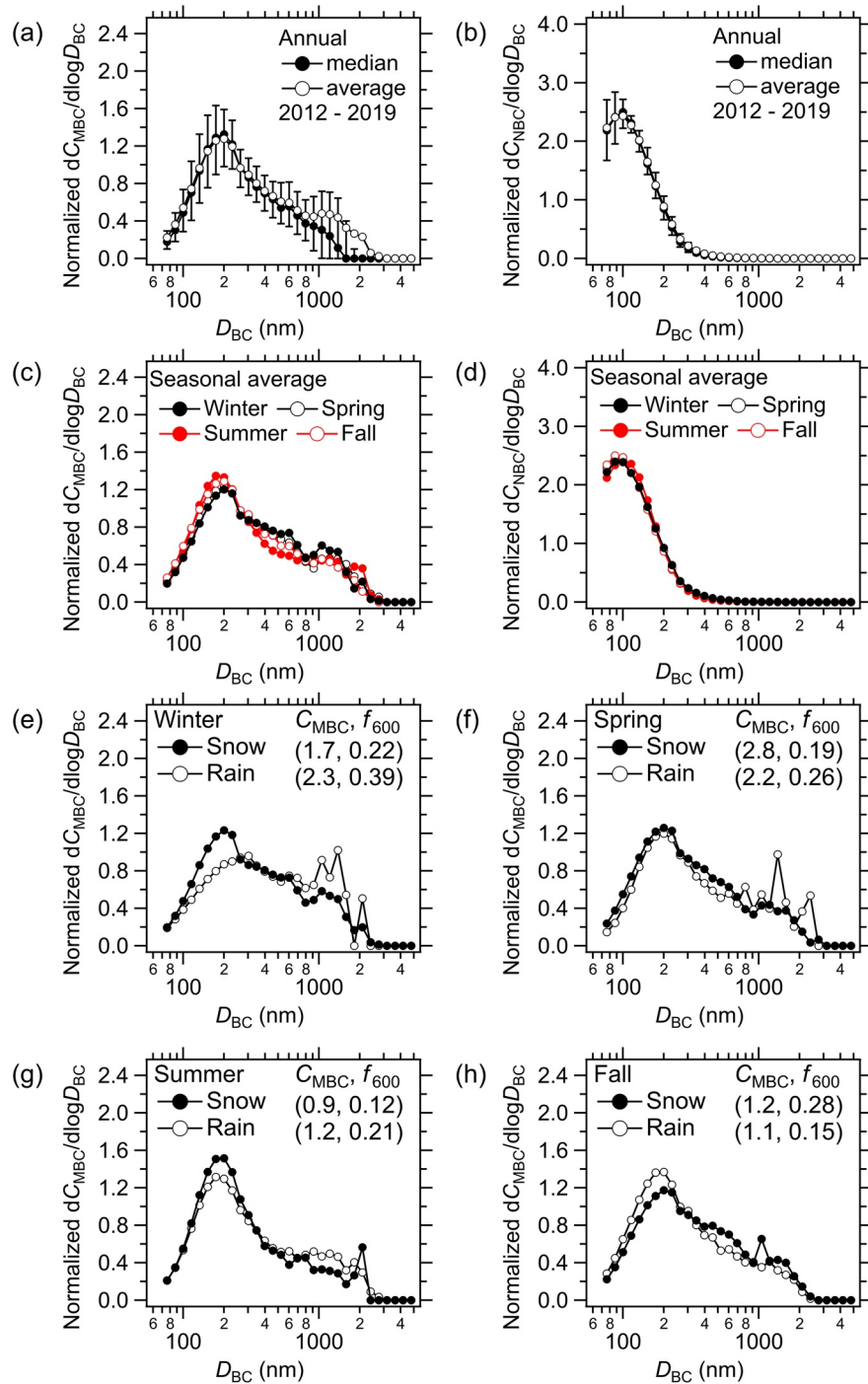


Figure 9. (a) Annual median and average black carbon (BC) mass and (b) BC number size distributions in hydrometeors at Ny-Ålesund during 2012–2019, normalized by total C_{MBC} or C_{NBC} for each sample. Error bars indicate variabilities (25th and 75th percentiles) for the annual median BC size distributions in precipitation events. (c) Seasonal average BC mass and (d) BC number size distributions in hydrometeors at Ny-Ålesund during 2012–2019, normalized by total C_{MBC} or C_{NBC} for each sample. Also shown are seasonal average BC mass size distributions in hydrometeors on snow and rainy days during (e) winter, (f) spring, (g) summer, and (h) fall, normalized by total C_{MBC} for each precipitation event; seasonal median values of daily C_{MBC} ($\mu\text{g L}^{-1}$) and f_{600} for snow and rain events are also shown at the top of each panel.

Table 5
Seasonal Parameter Values for Snow, Rain, and all Sampling Days at Ny-Ålesund From August 2012 to October 2019

		MMD (nm)	CMD (nm)	σ_{gm}	σ_{gc}	f_{600}	m_{BC} (fg)
Snow days							
Winter	Median	224 (183, 307)	102 (88, 109)	1.8 (1.7, 2.0)	1.7 (1.6, 1.7)	0.22 (0.15, 0.42)	5.1 (3.7, 10)
	Average	269 ± 122	100 ± 16	1.8 ± 0.4	1.7 ± 0.2	0.28 ± 0.18	7.5 ± 6.1
Spring	Median	213 (185, 285)	97 (88, 106)	1.9 (1.8, 2.1)	1.6 (1.6, 1.7)	0.19 (0.13, 0.31)	4.9 (3.2, 7.0)
	Average	242 ± 83	105 ± 46	1.9 ± 0.3	1.6 ± 0.2	0.24 ± 0.16	5.9 ± 3.7
Summer	Median	193 (173, 230)	115 (109, 117)	1.7 (1.5, 1.9)	1.5 (1.5, 1.6)	0.12 (0.09, 0.29)	4.1 (3.2, 5.8)
	Average	214 ± 58	112 ± 16	1.8 ± 0.3	1.6 ± 0.1	0.21 ± 0.20	6.1 ± 5.3
Fall	Median	234 (194, 302)	92 (83, 102)	1.9 (1.7, 2.1)	1.7 (1.6, 1.7)	0.28 (0.16, 0.39)	5.1 (4.0, 7.9)
	Average	261 ± 104	97 ± 20	1.9 ± 0.4	1.7 ± 0.2	0.27 ± 0.15	6.3 ± 3.8
Rain days							
Winter	Median	313 (285, 328)	77 (73, 80)	2.4 (1.9, 2.6)	1.8 (1.7, 1.8)	0.39 (0.29, 0.48)	6.3 (5.4, 7.3)
	Average	308 ± 54	76 ± 6	2.1 ± 0.8	1.8 ± 0.1	0.39 ± 0.10	6.5 ± 1.4
Spring	Median	214 (198, 259)	107 (89, 120)	1.8 (1.8, 1.9)	1.6 (1.5, 1.6)	0.26 (0.12, 0.38)	5.9 (4.4, 7.9)
	Average	251 ± 98	105 ± 19	1.9 ± 0.4	1.6 ± 0.2	0.33 ± 0.27	9.6 ± 11
Summer	Median	200 (179, 239)	110 (96, 117)	1.7 (1.6, 1.9)	1.6 (1.5, 1.6)	0.21 (0.11, 0.40)	4.8 (3.5, 6.8)
	Average	222 ± 70	107 ± 14	1.7 ± 0.4	1.6 ± 0.1	0.27 ± 0.20	6.2 ± 5.1
Fall	Median	196 (171, 239)	96 (87, 116)	1.7 (1.6, 1.9)	1.6 (1.5, 1.7)	0.15 (0.09, 0.27)	4.0 (2.9, 6.6)
	Average	214 ± 77	102 ± 21	1.7 ± 0.4	1.6 ± 0.1	0.21 ± 0.16	5.6 ± 5.0
All sampling days							
Winter	Median	234 (188, 321)	98 (85, 109)	1.8 (1.7, 2.1)	1.7 (1.6, 1.7)	0.24 (0.15, 0.42)	5.3 (3.8, 9.2)
	Average	271 ± 116	99 ± 17	1.8 ± 0.5	1.7 ± 0.1	0.28 ± 0.18	7.3 ± 5.8
Spring	Median	214 (189, 295)	96 (89, 110)	1.9 (1.8, 2.2)	1.6 (1.6, 1.7)	0.20 (0.13, 0.33)	5.0 (3.4, 7.9)
	Average	252 ± 96	105 ± 43	1.9 ± 0.3	1.6 ± 0.2	0.26 ± 0.18	6.6 ± 5.2
Summer	Median	199 (178, 239)	111 (96, 117)	1.7 (1.6, 1.9)	1.6 (1.5, 1.6)	0.21 (0.10, 0.39)	4.6 (3.4, 6.6)
	Average	220 ± 68	107 ± 15	1.7 ± 0.3	1.6 ± 0.1	0.26 ± 0.20	6.2 ± 5.1
Fall	Median	209 (173, 261)	93 (83, 111)	1.7 (1.6, 2.0)	1.6 (1.6, 1.7)	0.21 (0.10, 0.33)	4.4 (3.1, 6.9)
	Average	239 ± 126	100 ± 21	1.8 ± 0.4	1.6 ± 0.2	0.24 ± 0.17	6.1 ± 5.7

Note. MMD, mass median diameter; CMD, count median diameter; σ_{gm} and σ_{gc} , geometric standard deviations for the mass and number size distributions; f_{600} , ratio of BC mass concentration (integrated from $D_{BC} = 600$ nm to 4,170 nm) to total C_{MBC} (integrated from $D_{BC} = 70$ nm to 4,170 nm); m_{BC} , BC mass per particle. Median values include 25th and 75th percentiles in parentheses; average values include $\pm 1\sigma$. Data from snow samples collected by windsock from September 2012 to June 2016 are not included.

although the C_{MBC} and C_{NBC} were higher by a factor of 2 and 3, respectively, and the MMD was somewhat lower.

Figure 10a shows the daily average BC number size distributions in ambient air and falling snow on the three precipitation days, along with their combined averages; the corresponding BC mass size distributions are shown in Figure 10b. First, the ratio of the normalized number size distribution for BC in snow ($dC_{NBC}(D_{BC})/d\log D_{BC}$) to that in air ($dN_{BC}(D_{BC})/d\log D_{BC}$) was derived as

$$R(D_{BC}) = \left[dC_{NBC}(D_{BC}) / d\log D_{BC} \right] / \left[dN_{BC}(D_{BC}) / d\log D_{BC} \right]. \quad (2)$$

This size-resolved removal efficiency, normalized to an average value of unity, is referred to as $RE(D_{BC})$ and is shown in Figure 10a.

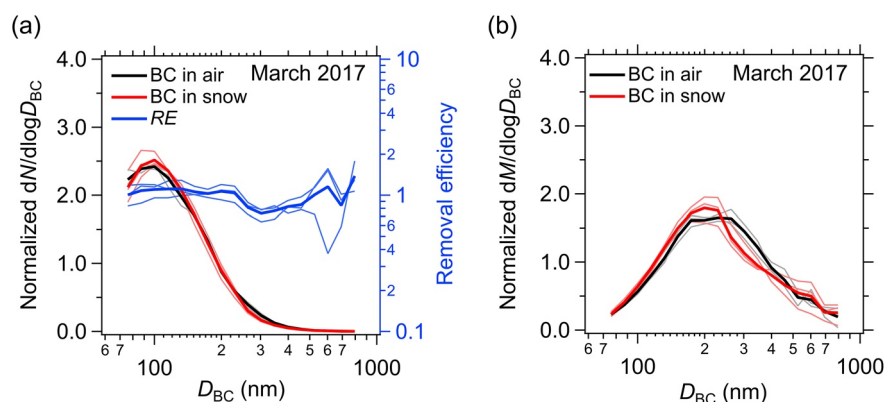


Figure 10. (a) Black carbon (BC) number size distributions in air and snow and BC removal efficiency (RE) within the 70–850 nm D_{BC} range for three precipitation events (thin lines) and their average (bold lines) during March 2017. The ratio of the normalized number size distribution of BC in snow to that of BC in air was calculated first, and $RE(D_{BC})$ was derived by normalizing this ratio. See the text for more details. (b) BC mass size distributions in air and snow for the same precipitation events. The size distributions in (a) and (b) are normalized by the total C_{NBC} or C_{MBC} .

The RE for BC between $D_{BC} = 70$ and 850 nm depended little on particle size, indicating that the shapes of the BC size distributions in ambient air at the altitude of Zeppelin Observatory and in falling snow were very similar. BC sizes in hydrometeors should be affected by those in ambient air not only at the surface, but also in the lower free troposphere (Mori et al., 2020). The monthly P -weighted C_{MBC} was not directly linked with the near-surface M_{BC} at Ny-Ålesund, as discussed in Section 4.2. Despite possible spatial variability in M_{BC} , this result suggests that the BC size distributions have similar shapes, on average, from the PBL to the lower troposphere over Ny-Ålesund.

4.5.3. Removal Efficiency of BC

In general, aerosol particles are more efficiently activated as cloud condensation nuclei (CCN) as their size and hygroscopicity increase (Petters & Kreidenweis, 2007). Thus, the RE for BC is strongly influenced by the microphysical properties of BC-containing particles (e.g., their mixing state and size) because wet removal of aerosols is mainly controlled by the activation of aerosols to cloud droplets (Moteki et al., 2019; Ohata, Moteki et al., 2016). Aerosol particles are also scavenged by collisions with water and ice particles within clouds and falling hydrometeors, as discussed later in this section.

The median shell-to-core ratio was found to be about 1.2 in the urban atmosphere of Tokyo in Japan, where aerosols were dominantly organic matter, and $RE(D_{BC})$ decreased with decreasing D_{BC} (Ohata, Moteki et al., 2016; Ohata, Schwarz, et al., 2016). This finding indicates that smaller BC-containing particles are not efficiently activated as CCN. On the other hand, the median shell-to-core ratio at a site strongly influenced by outflow from the East Asian continent, where the chemical composition of $PM_{2.5}$ is dominantly sulfate, was found to be about 1.4, and $RE(D_{BC})$ depended little on particle size within the 70–850 nm D_{BC} range (Moteki et al., 2019; Yoshida et al., 2020), as discussed in more detail in Section 5.5. This suggests that aged BC-containing particles with $D_{BC} = 70$ nm can be activated.

At Zeppelin Observatory, the median shell-to-core ratio of airborne BC particles was about 1.3 during the three March 2017 precipitation events. Ambient aerosol particles were routinely collected each day at Zeppelin Observatory by using a filter-pack sampler with no size cutoff and the mass concentrations of inorganic ions (e.g., SO_4^{2-} , NO_3^- , Na^+ , Mg^{2+} , and Cl^-) were measured by ion chromatography. In addition, mass concentrations of organic carbon (OC), collected with a high-volume sampler with a PM_{10} impactor on a biweekly basis, were measured by a thermal-optical transmittance analyzer (Sunset Laboratory, Tigard, OR) (Aas et al., 2019). The mass concentration of non-sea-salt sulfate is derived from concentrations of Na^+ , Mg^{2+} , and Cl^- (Hawley et al., 1988; Keene et al., 1986). These aerosol datasets are available at the Norwegian Institute for Air Research (NILU) data archive (<http://ebas.nilu.no/>). From February to April 2017, non-sea-salt sulfate accounted for about 66% of the total aerosol mass concentration (i.e., non-sea-salt sulfate,

nitrate, and OC). These data were used to estimate the effect of hydrophilic compounds on activation of BC-containing particles into cloud droplets, as discussed below.

The activation of aerosols also depends on the maximum water supersaturation in ambient air. Koike et al. (2019) reported that supercooled water droplets had number concentrations close to those of aerosol particles with dry diameters larger than about 70 nm at Zeppelin Observatory in the summer and winter-spring seasons of 2013–2015, indicating that such aerosols were activated during those seasons. In addition, for the summertime data, they estimated the maximum supersaturation in ambient air by using an air parcel model that thermodynamically calculates cloud particle formation from aerosols within an ascending air parcel, based on the number size distributions of aerosols and cloud droplets and an assumed aerosol composition of ammonium sulfate and updraft velocities of 6–20 cm s⁻¹ (Koike et al., 2019). The observed monthly median aerosol number concentrations (70–809 nm) during the summers of 2013–2015 were very low (<120 cm⁻³) at Zeppelin Observatory (Koike et al., 2019), indicating relatively high maximum supersaturations (>0.3%) in ambient air depending on the updraft velocity. Jung et al. (2018) also reported, on the basis of simultaneous measurements of number concentrations of aerosol and CCN at Zeppelin Observatory during 2007–2013, that all accumulation mode aerosol particles (60–300 nm) were active as CCN at maximum supersaturations of about 0.2% or higher throughout the year.

We estimated critical supersaturations of BC-containing particles as was done by Ohata, Schwarz, et al. (2016). For this estimate, first, the volume fraction of BC core and BC-containing material was derived from the measured shell-to-core ratio of 1.3. Then we calculated the hygroscopicity parameter κ (Petters & Kreidenweis, 2007) of BC coating material. We made four assumptions for this calculation: (a) the chemical composition of BC coating is the same as that of non-BC aerosols composed of non-sea-salt sulfate, nitrate, and organic matter (OM); (b) mass ratios of OM to OC range from 1.2 to 2.4 (e.g., Aiken et al., 2008; Russell, 2003); (c) κ values of OM range from 0.0 to 0.12 (Latham et al., 2013; Petters & Kreidenweis, 2007); and (d) the density of OM is about 1.4 g cm⁻³ (e.g., Kuwata et al., 2012).

The κ values of BC-containing particles were 0.35–0.40 and 0.24–0.32 for OM/OC ratios of 1.2 and 2.4, respectively, within the 0.0–0.12 range of κ values for OM. By using κ -Köhler theory (Petters & Kreidenweis, 2007), we calculated the critical supersaturation of BC-containing particles with $D_{BC} = 186$ nm to be 0.07%–0.09% for OM/OC ratios of 1.2–2.4. We also calculated the critical supersaturation of BC-containing particles with $D_{BC} = 70$ nm by estimating their median shell-to-core ratio. The shell-to-core ratio at $D_{BC} = 70$ nm was obtained by extrapolation from $D_{BC} = 186$ nm, assuming condensation of sulfuric acid vapor on the surface of BC particles, as described in detail elsewhere (Mori, 2017; Seinfeld & Pandis, 2016). The calculated median shell-to-core ratio for $D_{BC} = 70$ nm was 1.42, yielding a critical supersaturation of 0.26%–0.33% for OM/OC ratios of 1.2–2.4. These estimates were comparable to or lower than the observed maximum water supersaturations. These results suggest that aged BC-containing particles as small as $D_{BC} = 70$ nm are removed mainly by activation into cloud droplets.

Impaction processes also remove aerosol particles, by collisions between aerosol and cloud particles (water and ice) within clouds and by collisions between aerosol particles and falling hydrometeors below clouds, mainly by Brownian diffusion, interception, and inertial impaction (Wang et al., 2010; Zhang et al., 2013). According to theoretical and experimental studies, the collection efficiency of aerosol particles scavenged in these two settings is low within the 100–3,000 nm aerodynamic diameter range (Wang et al., 2010; Zhang et al., 2013), depending on the sizes and shapes of falling hydrometeors. Moteki et al. (2019) measured the size-resolved *RE* of BC for 37 rainfall events in East Asia and estimated the relative contributions of nucleation scavenging, in-cloud impaction scavenging, and below-cloud impaction scavenging by using a cloud parcel model including aerosol-cloud impaction processes. The fractional contribution of nucleation scavenging was greater than 0.8 within a 200–2,000 nm D_{BC} range. In midlatitudes, the contributions of in-cloud and below-cloud impaction scavenging increase at $D_{BC} < 200$ nm to some extent, due to the lower maximum supersaturation in ambient air (~0.08%) (Moteki et al., 2019). However, at Ny-Ålesund where the maximum supersaturation is higher (>0.3%), as discussed above, BC-containing particles would be removed mainly by nucleation scavenging.

It should be noted that large fractions of BC are transported from lower latitudes, as shown by trajectory analyses (Eleftheriadis et al., 2009; Liu et al., 2015) and model calculations (AMAP, 2015; Hirdman

Table 6
Annual Median Values at Ny-Ålesund From August 2012 to October 2019 and Barrow From July 2013 to August 2017 and Their Ratio (Barrow/Ny-Ålesund)

	M_{BC} (ng m ⁻³)	P -weighted C_{MBC} (μg L ⁻¹)	P -weighted C_{NBC} (μ L ⁻¹)	P (mm month ⁻¹)	F_{MBC} (μg m ⁻² month ⁻¹)	F_{NBC} (10 ⁹ m ⁻² month ⁻¹)	MMD (nm)	CMD (nm)	σ_{gm}	σ_{gc}	f_{600}	m_{BC} (fg)
Ny-Ålesund	6.6	1.9	415	34	65	14	209	100	1.8	1.6	0.21	4.8
Barrow	12	5.4	947	11	62	10	234	98	1.8	1.7	0.21	5.2
Ratio	1.8	2.8	2.3	0.3	1.0	0.7	1.1	1.0	1.0	1.1	1.0	1.1

et al., 2010). We show in Section 5.5 that freshly emitted BC particles become thickly coated during transport from their source regions. Therefore, it is likely that the CCN activities of BC-containing particles in the Arctic are largely set before they reach the Arctic, although the particles are further processed in the Arctic. Therefore, it seems natural that the CCN activities of BC-containing particles are high in general.

5. Comparison of BC Wet Deposition at Ny-Ålesund and Barrow

In this section, we describe BC wet deposition at Ny-Ålesund (2012–2019) and Barrow (2013–2017) on the basis of M_{BC} , C_{MBC} , P , F_{MBC} , and size distribution. These parameters at Barrow are summarized in Mori et al. (2020). For comparison, we used the median of 87 monthly values at Ny-Ålesund during 2012–2019 and that of 35 monthly values at Barrow during 2013–2017 for each parameter, referred to here as the annual median. The annual median values for these and other parameters at Ny-Ålesund and Barrow are summarized in Table 6.

5.1. BC Mass Concentration in the PBL

Median monthly M_{BC} at Ny-Ålesund and Barrow had similar seasonal variations, high in winter and spring and low in summer (Figure 5a). Analysis of backward trajectories starting from Zeppelin Observatory during 2002–2007 has shown that polluted air masses were commonly transported from northern Eurasia during winter and relatively clean air masses were transported mainly from the northern Arctic during summer (Hirdman et al., 2010). At Barrow, 10-day backward trajectories from 925 hPa during 1989–2003 have shown that air masses were commonly transported from western and eastern Russia during winter and from the Pacific and western China-Pacific regions during summer (Sharma et al., 2006). In addition, radiosonde measurements in winter showed that average PBL heights at Ny-Ålesund (~640 m) and Barrow (~230 m) were higher than the altitudes of the observation sites. These results indicate that high M_{BC} during winter and spring at both sites were caused by the transport of polluted air masses from mid and high latitudes, and the accumulation of BC in the PBL. In addition, the low M_{BC} in summer results from enhanced BC wet deposition during long-range transport, as described in Section 4.1 (AMAP, 2015; Browse et al., 2012; Hirdman et al., 2010; Quinn et al., 2007; Sharma et al., 2006, 2013).

The annual median M_{BC} value at Ny-Ålesund was lower than at Barrow by a factor of 1.8 (Figure 5a and Table 6). The difference between these localities may arise from the difference in the distances from BC emission sources, the different observation altitudes, and the degrees of dilution through mixing and BC wet removal during transport of air from lower latitudes.

5.2. BC Mass Concentration in Hydrometeors

Median monthly P -weighted C_{MBC} at Ny-Ålesund are compared with that at Barrow in Figure 5b (C_{NBC} values are compared in Figure S1a). The annual median P -weighted C_{MBC} was lower at Ny-Ålesund than at Barrow by a factor of 2.8 (Figure 5b and Table 6). From January to May, the variations of C_{MBC} at the two sites were similar, although C_{MBC} was lower by factors of 2–3 at Ny-Ålesund (Figure 5b).

The variability of the monthly P -weighted C_{MBC} was generally larger at Barrow than at Ny-Ålesund, partly because Barrow had fewer data. The annual mean ($\pm 1\sigma$) value of the number of sampling days at Barrow was 8.4 ± 4.8 per month during 2013–2017 (Figure 5e and Table S1), which is about one-fifth that at Ny-Ålesund (46 ± 12). However, the relatively smooth seasonal variation of median monthly P -weighted C_{MBC}

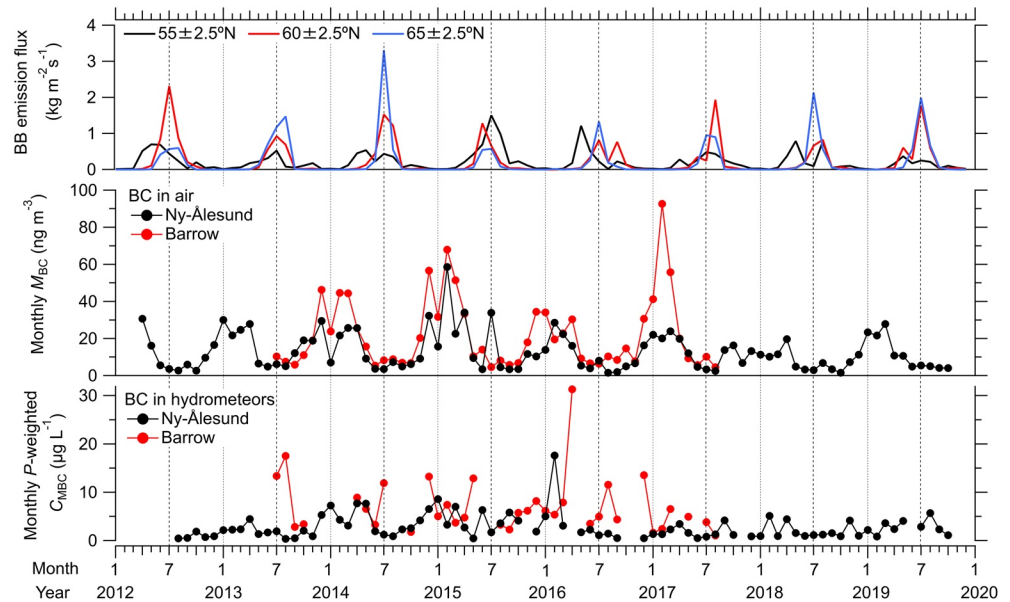


Figure 11. (upper) Monthly average values of zonally averaged biomass burning (BB) emission fluxes of black carbon (BC) at a horizontal resolution of 0.1° latitude/longitude in the Northern Hemisphere ($>55^\circ\text{N}$) during 2012–2019 from the Global Fire Assimilation System data set (Kaiser et al., 2012). (middle) Monthly average values of M_{BC} (BC in air) on all days at Ny-Ålesund (2012–2019) and Barrow (2013–2017). (lower) Monthly average values of P -weighted C_{MBC} (BC in hydrometeors) on precipitation days at Ny-Ålesund and Barrow.

and the similar seasonal patterns of monthly and daily data (not shown) suggest that the average seasonality of monthly P -weighted C_{MBC} is not strongly influenced by small data numbers, except for May, June, and November. The high variability in July and August is discussed below.

Median monthly values of P -weighted C_{MBC} and M_{BC} at Barrow were moderately correlated ($r^2 = 0.17$) except for July and August (Figure 6c), although the median monthly value was based on about three average values (Table S1). In addition, the median daily values of C_{MBC} and M_{BC} were also moderately correlated ($r^2 = 0.15$; Figure 6d) for days with $P > 0.5$ mm, which account for about 80% of the data. The r^2 values were lower at Barrow than at Ny-Ålesund (section 4.2).

In July and August, C_{MBC} at Ny-Ålesund decreased, as did M_{BC} ; however, C_{MBC} at Barrow remained high, while M_{BC} greatly declined which suggests that C_{MBC} did not directly reflect M_{BC} near the surface (Figure 5b). Mori et al. (2020) sought to explain this discrepancy at Barrow by estimating the contributions of C_{MBC} separately for anthropogenic and biomass burning emissions using two different global models. The model calculations showed that M_{BC} increases in the free troposphere in summer due to BC emissions from biomass burning and that BC particles are removed by precipitation below ~ 2 km. This result suggests that the high C_{MBC} at Barrow is strongly influenced by increased M_{BC} in the lower troposphere from biomass burning emissions.

To investigate the effects of biomass burning on C_{MBC} at Ny-Ålesund during summer, we used the Global Fire Assimilation System data set (Kaiser et al., 2012) to calculate zonally averaged biomass burning emission fluxes for three latitude bands ($55^\circ\text{N} \pm 2.5^\circ\text{N}$, $60^\circ\text{N} \pm 2.5^\circ\text{N}$, and $65^\circ\text{N} \pm 2.5^\circ\text{N}$) at a horizontal resolution of 0.1° latitude/longitude, and compared the results with monthly M_{BC} and P -weighted C_{MBC} at Ny-Ålesund and Barrow (Figure 11). The biomass burning emission fluxes reached their maximum during July and August, corresponding to the seasonal pattern of C_{MBC} at Barrow (Figure 5b), whereas the monthly P -weighted C_{MBC} at Ny-Ålesund was much lower during those two months. This result suggests that the effect of biomass burning on C_{MBC} is much smaller at Ny-Ålesund than at Barrow, possibly because of transport of cleaner air masses in the lower free troposphere over Ny-Ålesund, although we made no quantitative analysis of the potential effect of biomass burning in this study. Note that daily C_{MBC} values were sometimes

high at Ny-Ålesund during summer of 2015, 2016, and 2019 (Figure 3), which may have arisen from occasional transport of air parcels influenced by biomass burning.

The two global model calculations by Mori et al. (2020) showed that the correlation between monthly C_{MBC} and M_{BC} near the surface at Barrow was relatively poor, whereas the monthly BC column amount and C_{MBC} were well correlated, suggesting that monthly C_{MBC} is more strongly controlled by M_{BC} in the free troposphere over Barrow than by M_{BC} near the surface. Thus, the observed poor correlation between monthly C_{MBC} and M_{BC} at Ny-Ålesund may also arise from differences in the variations of monthly M_{BC} in the free troposphere and in the PBL. It should also be noted that the model calculations had a horizontal spatial resolution of about 100–200 km (Matsui et al., 2018; Oshima et al., 2020). This resolution would smooth the variability in C_{MBC} and M_{BC} , possibly leading to stronger correlations than those observed. This point is important in comparing model calculations with the in-situ data.

5.3. Precipitation and BC Wet Deposition Flux

Median monthly P at Ny-Ålesund was low in summer and high in winter, whereas at Barrow it was high from late spring to early fall (Figure 5c). During winter, the median monthly P value at Ny-Ålesund was about eight times greater than at Barrow, whereas in summer the P values at Ny-Ålesund and Barrow were comparable. Annual median P values were about 3 times greater at Ny-Ålesund than at Barrow (Figure 5c and Table 6).

The seasonal variations of median monthly F_{MBC} had very different patterns at Ny-Ålesund and Barrow, corresponding to their differences in C_{MBC} and P (Figure 5d). The seasonal patterns of F_{MBC} and F_{NBC} were similar for each site (Figure S1c). At Ny-Ålesund, median monthly F_{MBC} was highest in winter, whereas it was highest in summer at Barrow. The amount of BC wet deposition per unit area was 0.71 mg m^{-2} at Barrow during summer (Mori et al., 2020), which is comparable to our estimate for Ny-Ålesund during winter (0.58 mg m^{-2}). The annual median F_{MBC} values at Ny-Ålesund ($65 \mu\text{g m}^{-2} \text{ month}^{-1}$) and at Barrow ($62 \mu\text{g m}^{-2} \text{ month}^{-1}$) were also comparable (Figure 5d and Table 6).

5.4. Size Distributions

The annually and seasonally averaged BC mass size distributions in hydrometeors were very similar at Ny-Ålesund and Barrow, and the annually averaged BC number size distributions at both sites were also similar (Figure 12). Annual median values of the parameters MMD, CMD, σ_{gm} , σ_{gc} , f_{600} , and m_{BC} at Ny-Ålesund agreed with those at Barrow within 10% (Table 6). These similarities are striking, considering the differences between Ny-Ålesund and Barrow in the concentrations of BC (M_{BC} and C_{MBC}), meteorological conditions (P), emission sources, and transport pathways and the large distance between the two sites (Figure 1). In this section, we attempt to explain these features and relate the size distributions of BC in hydrometeors at Ny-Ålesund and Barrow with those measured in the atmosphere at Ny-Ålesund.

5.4.1. Microphysical Properties of BC and Supersaturation

As described in Section 4.5.2, the BC size distributions in air and falling snow at Ny-Ålesund in spring 2017 were very similar, showing that RE of BC within the 70–850 nm D_{BC} range was size-independent because of the efficient activation of BC-containing particles into cloud droplets. This size independence is consistent with the microphysical properties of BC and supersaturations observed by aircraft observations in the Arctic, as summarized below.

PAMARCMiP aircraft observations in spring 2018 showed that BC particles at 0.2–5.2 km altitudes north of 78°N were thickly coated, with median shell-to-core ratios of 1.35–1.45 in the 186–236 nm D_{BC} range (Yoshida et al., 2020). Thickly coated BC-containing particles were also dominant below 4 km over the Canadian High Arctic region in summer 2014 (72.5°N–77.5°N, 100°W–80°W) and spring 2015 (80°N–85°N, 105°W–60°W) in observations of the NETCARE aircraft campaign (Kodros et al., 2018). These results strongly suggest that BC particles are thickly coated in general in the Arctic.

The degree of activation of aerosol particles into cloud droplets has also been studied by aircraft observations in the Arctic (Leaitch et al., 2016). The NETCARE aircraft campaign in summer 2014 measured number

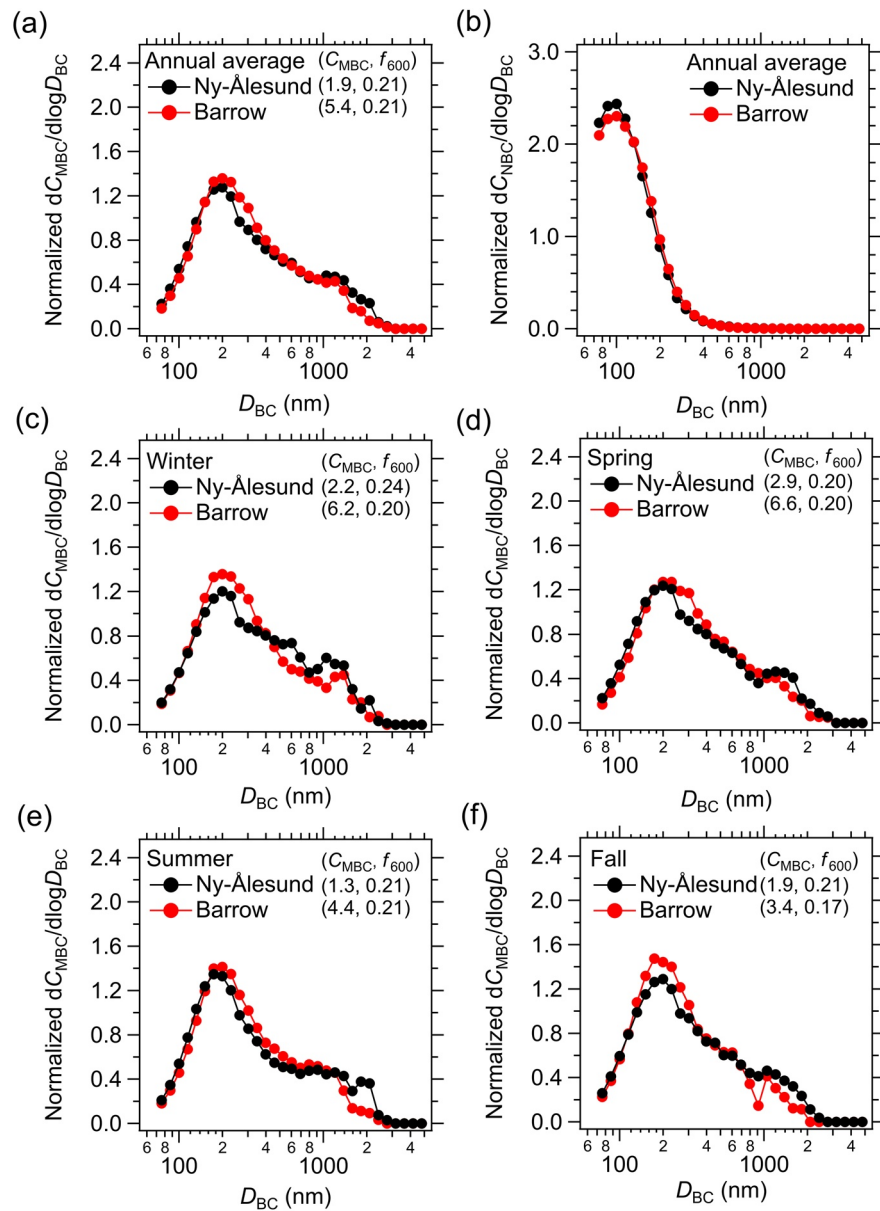


Figure 12. Annual average (a) black carbon (BC) mass and (b) BC number size distributions in hydrometeors at Ny-Ålesund (black) and Barrow (red) and seasonal average BC mass size distributions in hydrometeors at Ny-Ålesund and Barrow during (c) winter, (d) spring, (e) summer, and (f) fall, normalized by total C_{MBC} or C_{NBC} for each precipitation event. Annual and seasonal median values of monthly P -weighted C_{MBC} ($\mu\text{g L}^{-1}$) and f_{600} are shown at the top of each mass size distribution panel. BC size distributions at Barrow during fall were calculated after excluding data with $f_{600} > 0.31$ (Mori et al., 2020).

concentrations of cloud droplets and CCN and showed high supersaturation (0.3%–0.6%) in ambient air at 0.06–6.0 km altitudes in the Canadian High Arctic (Leaith et al., 2016). The observed high supersaturation is comparable to that observed at Zeppelin Observatory (Koike et al., 2019).

The aircraft observations during PAMARCMiP 2018 and NETCARE 2015 documented an altitude dependence of BC size distributions in spring (Schulz et al., 2019; Yoshida et al., 2020), in which the MMD of BC at high latitudes ($>70^\circ\text{N}$) gradually decreases from 200 nm at 1 km to 150 nm at 5 km.

5.4.2. Altitudes of BC Wet Removal and Altitude Dependence of BC Size

Global model calculations by Mori et al. (2020) showed that BC wet removal occurs mainly at altitudes below ~2 km at Barrow throughout the year. The altitudes of BC wet removal were calculated to be similar at Ny-Ålesund (not shown).

The change in MMD for BC size distributions from the PBL to the lower troposphere (<2 km) was small (190–200 nm) over the Canadian High Arctic in summer 2014 and spring 2015 (Schulz et al., 2019).

5.4.3. BC Size Distributions in the Lower Troposphere

Combining these observations and model calculations (Sections 5.4.1 and 5.4.2), it appears likely that the shapes of the BC size distributions in hydrometeors reflected those in the lower troposphere at Ny-Ålesund and Barrow. Therefore, it is likely that the average shapes of BC size distributions from the surface to the lower troposphere were also similar at the two sites.

Note that BC size distributions in the lower troposphere may not be uniform at lower latitudes. Mori et al. (2019) investigated the latitudinal dependence on the size of BC particles deposited on Arctic snow in the latitude band 60°N–80°N, where local BC emissions are negligible during the snow accumulation period, and reported that BC size distributions in snowpack shifted toward larger sizes at lower latitudes.

5.5. Processes That Control BC Size Distributions in the Arctic

The annual median (25th percentile, 75th percentiles) f_{1000} values were 0.09 (0.03, 0.21) at Ny-Ålesund and 0.09 (0.06, 0.15) at Barrow, indicating that a substantial BC mass was in the super-micron range ($D_{BC} > 1,000$ nm) in hydrometeors; therefore, f_{1000} was also similar in the lower troposphere throughout the year. Super-micron BC particles have also been found in the Arctic and Antarctic in hydrometeors, surface snow, and snowpack (Kinase et al., 2020; Marquette et al., 2020; Mori et al., 2019, 2020; Sinha et al., 2018). Generally, larger BC particles should be removed more efficiently due to their presumably higher CCN activities. However, the ubiquitous existence of super-micron BC is apparently inconsistent with this supposition. We need to reconcile this feature with our understanding of the processes that control BC size distributions and mixing states. In this section, we consider three of these processes on the basis of observations of microphysical properties and wet removal of BC at urban and remote sites in East Asia (Mori et al., 2016; Moteki et al., 2019; Ohata, Moteki et al., 2016; Yoshida et al., 2020).

5.5.1. Ground-Based Measurements of BC in East Asia

Previous studies have measured the size distributions of BC in air and rainwater for 29 precipitation events in urban Tokyo during the summers of 2014–2015 (Mori et al., 2016; Moteki et al., 2019; Ohata, Moteki et al., 2016), for six events on Fukue Island in the spring of 2019 (Yoshida et al., 2020), and for 11 events at Cape Hedo in Okinawa during the spring of 2016 (Moteki et al., 2019), as shown in Figure 13. Fukue and Cape Hedo are in the East China Sea about 250–600 km and 800–1,000 km from the coasts of the Asian continent (China and Korea), respectively (Figure 28 of Kondo, 2015). They are strongly influenced by Asian outflows and little influenced by local BC emission sources (Kondo, 2015; Shiraiwa et al., 2008). Typical transport times of air parcels from the Asian continent in spring are about 1–2 days to Fukue and about 2–3 days to Hedo (Kondo et al., 2016; Shiraiwa et al., 2008). Figure 13d shows the RE at all three sites, and the median values of BC shell-to-core ratios for $D_{BC} = 186$ nm are summarized in Table 7. In Tokyo, the RE increased with D_{BC} , indication of thin coating. This size dependence of RE was much weaker at Fukue and Hedo, where BC particles were thickly coated. At Hedo, RE was independent of D_{BC} , similar to the case at Ny-Ålesund (section 4.5.3).

Process 1 RE in an air parcel becomes size-independent by BC aging during transport, unless fresh BC particles are added to the parcel.

5.5.2. Transport of BC to the Arctic PBL and Lower Troposphere

Transport of BC to the Arctic in the PBL is most efficient in winter and spring, when the edge of the polar dome shifts as far south as 40°N (AMAP, 2015; Barrie, 1986). North of 40°N, BC is emitted mainly at 40°N–60°N and is transported in the cold PBL over long distances. BC can also reach the Arctic lower

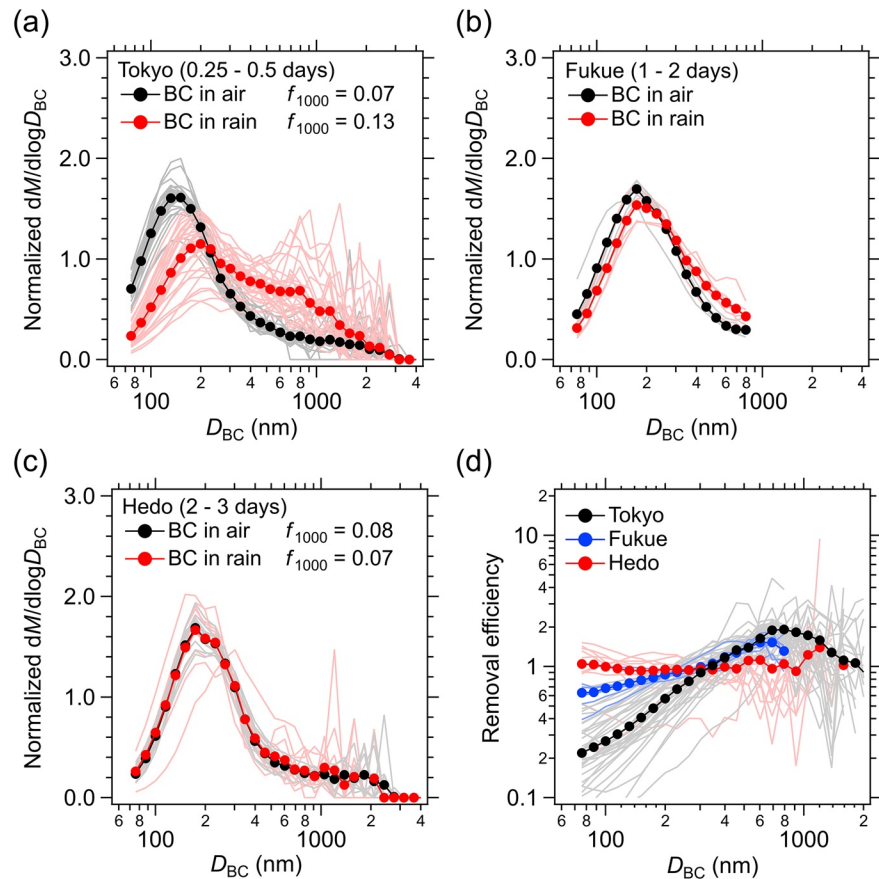


Figure 13. Normalized mass size distributions of black carbon (BC) in air and rainfall (a) for 29 precipitation events in Tokyo during the summers of 2014 and 2015, (b) for six events at Fukue Island during spring 2019, and (c) for 11 events at Cape Hedo on Okinawa Island during spring 2016. Typical transport times of air parcels from BC sources are shown at the top of each panel. Average ratios of C_{MBC} for super-micron BC particles ($D_{BC} = 1,000\text{--}4,170$ nm) to total C_{MBC} (f_{1000}) for all precipitation events are also shown at the top of (a) and (c). (d) Removal efficiency of BC at the three sites, normalized by the average removal efficiency within the $D_{BC} = 70\text{--}2,000$ nm range. Thick curves show their averages over all precipitation events at the three sites.

troposphere by ascending over the polar dome (AMAP, 2015; Browse et al., 2012). These BC particles generally are continuously coated by non-BC (inorganic and organic) species during transport through condensation and coagulation processes, unless fresh BC particles are added to the air parcel through significant injections or mixing events. At some stage, the BC size distributions in a parcel reach a stable shape, even after precipitation events, because RE becomes size-independent, although the BC mass concentrations change. In fact, BC in the Arctic ($>70^\circ\text{N}$) is thickly coated (Section 5.4.1). Thus, BC size distributions would tend to have stable shapes in the Arctic PBL and lower troposphere, and super-micron BC particles would be ubiquitous there. Here, we assumed that wet deposition predominates over dry deposition for the supermicron BC particles because aerosol particles as large as a few micrometers have low settling velocities (Seinfeld & Pandis, 2016).

Table 7

Median Values of Shell-to-Core Ratio for $D_{BC} = 186$ nm at Several Sites in East Asia

Observation site (latitude, longitude)	Altitude (m)	Year	Season	Shell-to-core ratio
Tokyo (35.7°N, 139.7°E)	20	2014–2015	Summer	1.19
Fukue (32.8°N, 128.7°E)	90	2019	Spring	1.45
Hedo (26.9°N, 128.3°E)	60	2016	Spring	1.37

This stabilizing process, together with horizontal and vertical mixing during transport, leads to uniform BC size distributions in the Arctic lower troposphere. Because BC removal is no longer size-selective, supermicron BC particles are widespread there.

Process 2 The BC size distribution stabilizes from the surface to the lower troposphere at higher latitudes, although vertical mixing may decrease the altitude dependence of the size distribution.

5.5.3. Aircraft Measurements in East Asia

Aircraft observations over the East China Sea have shown that the size distributions of BC in the free troposphere shift to smaller sizes with increasing altitude, as a result of wet removal over the East Asian continent (Kondo et al., 2016; Moteki et al., 2012). The majority of these BC particles were uplifted from the PBL into the free troposphere over large sources in China. Over China, BC particles in the PBL have younger average ages than at Hedo because of continued BC emissions in China, which leads to size-dependent *RE*, as observed in Tokyo (Figure 13d). At higher altitudes, BC undergoes greater wet removal, on average, and the average BC size decreases with altitudes (Kondo et al., 2016). Size-dependent *RE* accounts for the observed altitude dependence of the BC size distributions.

Process 3 Smaller BC particles are transported more efficiently to higher altitudes, when they are uplifted from the PBL to the free troposphere over large continental sources.

5.5.4. Transport of BC in the Arctic Free Troposphere

BC size distributions shift toward smaller sizes with increased altitude (1–5 km) at $>70^{\circ}\text{N}$ (Section 5.4.1). BC particles emitted south of the Arctic front can reach the Arctic middle or upper troposphere across surfaces of constant potential temperature (AMAP, 2015). Process 3 makes it likely that the altitude dependence of BC size distributions observed in the Arctic is mainly inherited from continental BC sources at lower latitudes, although the shape of the size distributions may depend to some extent on the type of BC source (Schwarz et al., 2008).

Our discussion is based on observations of BC in East Asia. However, processes 1–3 occur in all regions at various rates. An important point is that BC particles in source regions are linked with those in the Arctic by transport with time scales longer than the time scale of BC aging. It is very difficult to calculate the microphysical properties of BC by numerical models; however, qualitative understanding of the related processes will be useful in interpreting the observed results.

5.5.5. Seasonal Variation of BC Size Distributions

Precipitation at midlatitudes is generally highest in summer (e.g., Figure 8b), and thus BC size distributions would shift to smaller sizes more effectively in summer than in other seasons. This seasonal variation would propagate to the Arctic by long-range transport, causing the seasonal variations of BC size distributions in hydrometeors there.

In general, BC particles are more strongly influenced by biomass burning in summer than in other seasons (Section 5.2), and BC particles emitted from biomass burning have somewhat larger mean diameters than those from fossil fuel combustion (Kondo, Matsui et al., 2011; Schwarz et al., 2008). However, the influence of seasonal variations of BC wet removal on BC size distribution appears to be larger than the influence of biomass burning.

5.5.6. Effect of Atmospheric Circulation in the Arctic

Air parcels circulate in the Arctic ($>70^{\circ}\text{N}$), although they continually enter and exit the Arctic (Hirdman et al., 2010; Huang, Gong, Sharma, et al., 2010). This circulation may occasionally send similar air parcels over Ny-Ålesund and Barrow. The similarity of the BC size distributions at Ny-Ålesund and Barrow (Figure 12) may be influenced by the presence of similar types of air parcels, although the parcels arrive at different times. The variability in BC size distributions at the two sites, associated with the differences in sampling times is smoothed by time-averaging, which is done in producing Figure 12.

5.5.7. Effect of Coalescence of Cloud Droplets

After airborne BC-containing particles form cloud droplets, the droplets grow by water vapor condensation and by collisions between them (Straka, 2009). As a large droplet collects smaller droplets, it accumulates the BC particles in the small droplets by coalescence. If such a collector droplet evaporates without reaching the ground, the BC particles it contains can coagulate into a larger BC particle that is released to the atmosphere, as theorized by Moteki and Mori (2015) and demonstrated in laboratory studies by Mori et al. (2016).

BC size distributions may shift to larger sizes as this process is repeated during long-range transport from source regions to the Arctic. Although our discussion concerns liquid droplets, the processes of coalescence and evaporation apply similarly to ice particles. It is very difficult to quantify this effect given the complexity of these related processes in the atmosphere; however, the effect is limited to cloudy and precipitation days, whereas processes 1–3 occur readily in any sunlit region and therefore can be presumed to be more effective.

6. Summary and Conclusion

Wet deposition of BC is a key process controlling the spatial and temporal distribution of BC mass concentrations in air and snow. However, the scarcity of relevant measurements limits our understanding of BC distributions in hydrometeors and BC wet deposition in mixed-phase clouds in the Arctic. To better document BC wet deposition in the Arctic, we measured BC mass concentrations in air (M_{BC}) and in hydrometeors (C_{MBC}) with accuracies of 15% and 16%, respectively, at Ny-Ålesund from August 2012 to October 2019, along with meteorological parameters and cloud-base heights. We then compared our measurement parameters at Ny-Ålesund (M_{BC} , C_{MBC} , F_{MBC} , P , and BC size distributions in hydrometeors) with those at Barrow from 2013 to 2017 published by Mori et al. (2020).

Cloud-base height ranged from about 1–2 km with a clear seasonal variation, being high in winter and low in summer. The similar cloud-base temperatures at the two sites suggests that a portion of hydrometeors including BC originated in or passed through mainly mixed-phase clouds.

Median monthly M_{BC} and P -weighted C_{MBC} at Ny-Ålesund were highest in spring and lowest in summer. These two measurements were well correlated ($r^2 = 0.78$) in months with at least 40 data points during the study period. Thus, on a median monthly basis, the BC mass deposited per unit of precipitated water increases with increasing M_{BC} .

Wet deposition of BC (median monthly F_{MBC}) showed marked seasonal variation, being highest in winter ($96 \mu\text{g m}^{-2} \text{ month}^{-1}$) and lowest in summer ($28 \mu\text{g m}^{-2} \text{ month}^{-1}$), associated with the seasonal patterns of C_{MBC} and P . Wet deposition during winter accounted for about 35% of the annual wet deposition amount, reflecting higher precipitation in that season.

At Ny-Ålesund, the average BC size distributions in hydrometeors showed little temporal variation except in summer, and BC size distributions in hydrometeors on snow and rainy days were also similar. Size distributions of BC in hydrometeors and in ambient air measured in spring 2017 were very similar, suggesting that BC-containing particles with diameters larger than 70 nm were efficiently activated as CCN at Ny-Ålesund.

The median monthly M_{BC} at Ny-Ålesund and Barrow showed similar seasonal patterns, being highest during winter-spring and lowest in summer. By contrast, the median monthly P -weighted C_{MBC} at these sites showed different seasonal patterns, being low at Ny-Ålesund but high at Barrow during summer even as M_{BC} at the surface was low at both sites. Global model calculations have shown that the enhancement of C_{MBC} at Barrow is due to biomass burning (Mori et al., 2020). Considering this, our results suggest a lesser influence of biomass burning on C_{MBC} at Ny-Ålesund in summer, likely due to differences in the transport pathways of air parcels affected by biomass burning. Median monthly F_{MBC} at Ny-Ålesund and Barrow had different seasonal patterns due to different seasonal patterns of C_{MBC} and P at these sites.

Median monthly P -weighted C_{MBC} and M_{BC} at Barrow were moderately correlated ($r^2 = 0.17$) except for July and August. The lower r^2 value is partly due to the smaller number of data from Barrow than from Ny-Ålesund.

Annual median values of M_{BC} , C_{MBC} , P , and F_{MBC} at Ny-Ålesund were 6.6 ng m^{-3} , $1.9 \mu\text{g L}^{-1}$, 34 mm month^{-1} , and $65 \mu\text{g m}^{-2} \text{ month}^{-1}$, respectively. At Barrow, annual median values of M_{BC} , C_{MBC} , P , and F_{MBC} were 12 ng m^{-3} , $5.4 \mu\text{g L}^{-1}$, 11 mm month^{-1} , and $62 \mu\text{g m}^{-2} \text{ month}^{-1}$, respectively. Annual median M_{BC} and C_{MBC} values were lower at Ny-Ålesund than at Barrow by factors of about 2 and 3, respectively. On the other hand, the annual median P values were about 3 times higher at Ny-Ålesund than at Barrow. As a result, the two sites had comparable annual median F_{MBC} values.

BC particles observed at Ny-Ålesund in spring 2017 were thickly coated, indicating high CCN activity. In addition, previous aircraft observations have shown that BC particles are thickly coated in the Arctic PBL and free troposphere.

Annual and seasonal average BC size distributions in hydrometeors at Ny-Ålesund were very similar to those at Barrow. Considering the high CCN activities of BC-containing particles, the similarities suggest that BC size distributions from the PBL to the lower troposphere were also similar, on average, at these sites. This is a striking feature considering the large differences in environmental conditions and the distance between the two sites.

Measurements in East Asia have shown that the *RE* of BC becomes insensitive to BC size within 3–4 days after emission due to coating of BC by non-BC species. North of 40°N, BC is emitted mainly at 40°N–60°N and is transported to the Arctic in the PBL and lower troposphere over long distances in winter and spring. The measurements imply that BC particles continue to be coated by non-BC species during transport. At some stage, the BC size distributions attain a stable shape because *RE* becomes size-independent, and they tend to become uniform as mixing proceeds. This mechanism also explains the ubiquitous presence of super-micron BC, the seasonal variation of BC size distributions, and the mixing states of BC observed in the Arctic. Coalescence of BC by evaporation of cloud droplets may tend to slightly increase the size of BC particles.

Previous aircraft observations have shown that BC size distributions shift toward smaller sizes with increasing altitude between 1 and 5 km. BC particles emitted south of the Arctic front can reach the Arctic middle or upper troposphere across surfaces of constant potential temperature. It is likely that the altitude dependence of BC size distribution observed in the Arctic is mainly inherited from lower latitudes closer to the continental BC sources.

The reliable datasets of M_{BC} and F_{MBC} at Ny-Ålesund and Barrow will be useful for constraining and testing climate models. The BC size distributions in hydrometeors at Ny-Ålesund and Barrow will be useful in estimating the effect of BC on snow albedo in wide regions of the Arctic. More observations of M_{BC} in the lower troposphere, C_{MBC} , and F_{MBC} will further improve our quantitative understanding of the spatial and temporal distributions of BC deposited in the Arctic.

Appendix A: Controlling Factors of Variance of Wet Deposition Mass Flux of BC

Assuming that monthly *P*-weighted C_{MBC} and *P* are independent variables, the uncertainty in monthly F_{MBC} (σ_{FMBC}) is given as

$$(\sigma_{FMBC})^2 = \left(\frac{\partial F_{MBC}}{\partial C_{MBC}} \right)^2 (\sigma_{CMBC})^2 + \left(\frac{\partial F_{MBC}}{\partial P} \right)^2 (\sigma_P)^2 = (P)^2 (\sigma_{CMBC})^2 + (C_{MBC})^2 (\sigma_P)^2, \quad (A1)$$

where σ_{CMBC} and σ_P are 1σ uncertainties of monthly *P*-weighted average C_{MBC} and monthly *P* during 2012–2019, respectively. By dividing both sides in Equation A1 by $(F_{MBC})^2$, the relative uncertainty of monthly F_{MBC} is represented by the relative uncertainties of monthly C_{MBC} and *P*:

$$\left(\frac{\sigma_{FMBC}}{F_{MBC}} \right)^2 = \left(\frac{\sigma_{CMBC}}{C_{MBC}} \right)^2 + \left(\frac{\sigma_P}{P} \right)^2. \quad (A2)$$

We compared the relative uncertainties of monthly *P*-weighted C_{MBC} and *P* by using their averages and 1σ . The two relative uncertainties were comparable, suggesting that the variance of monthly F_{MBC} was controlled by both C_{MBC} and *P*, as might be expected. We also estimated the relative uncertainty of daily F_{MBC} during 2012–2019, showing that both daily C_{MBC} and *P* strongly control daily F_{MBC} .

Data Availability Statement

The authors used the cloud base height data from the NIPR database (<http://polaris.nipr.ac.jp/~aerosol01/Arctic/MPL/>), aerosol data of the Norwegian Institute for Air Research (NILU) from the EBAS database (<http://ebas.nilu.no/>), vertical profile data of meteorology from the National Climatic Data Center archive (<https://www.ncdc.noaa.gov/data-access/weather-balloon-data>), and AWS meteorological data from the Norwegian Meteorological Institute data set (<https://seklima.met.no/observations/>). Snow and rain samplings at Barrow were supported as part of the Atmospheric Radiation Measurement research program of the U.S. Department of Energy. The GPCP Precipitation data were provided by the NOAA/OAR/ESRL Physical Science Laboratory, Boulder, Colorado, USA (<https://psl.noaa.gov/>). The data used in this study are available at <https://ads.nipr.ac.jp/dataset/A20200923-001>.

Acknowledgments

The authors thank the staff of the Norwegian Polar Institute and J. Matsushita of the National Institute of Polar Research (NIPR) for supporting our continuous soot monitoring system (COSMOS) measurements and for collecting the snow samples at Ny-Ålesund. They acknowledge Walter Brower of UIC Science ARM for snow and rain sampling at Barrow. They also thank Bryan Thomas, Ross Peterson and Peter Detwiler of the U.S. National Oceanic and Atmospheric Administration for supporting our COSMOS measurements at Barrow. They thank AWIPEV engineers for maintaining MPL measurements and T. Terui of the NIPR for organizing the data transfer. This work was supported by the Japanese Ministry of Education, Culture, Sports, Science, and Technology (MEXT), the Environment Research and Technology Development Fund (JPMEERF20142003, JPMEERF20172003, JPMEERF20202003, and JPMEERF20205001) of the Environmental Restoration and Conservation Agency of Japan, Japan Society for the Promotion of Science KAKENHI Grants (JP12J06736, JP1604452, JP23221001, JP26241003, JP26701004, JP16H01770, JP17H04709, JP18H03363, JP18H04140, JP18H05292, JP19K20441, and JP20H00638), the Arctic Challenge for Sustainability (ArCS) project (JPMXD1300000000), the Arctic Challenge for Sustainability II (ArCS II) project (JPMXD1420318865), and a grant for the Global Environment Research Coordination System from the Ministry of the Environment, Japan (MLTI1753). MPL observations at Ny-Ålesund were registered by the Research in Svalbard (RiS) ID 3186 conducted by M. Shiobara (NIPR, Japan) in 2006–2018 and R. Neuber (AWI, Germany) in 2006–2020.

References

Aas, W., Mortier, A., Bowersox, V., Cherian, R., Faluvegi, G., Fagerli, H., et al. (2019). Global and regional trends of atmospheric sulfur. *Scientific Reports*, 9, 953. <https://doi.org/10.1038/s41598-018-37304-0>

Aiken, A. C., DeCarlo, P. F., Kroll, J. H., Worsnop, D. R., Huffman, J. A., Docherty, K. S., et al. (2008). O/C and OM/OC ratios of primary, secondary, and ambient organic aerosols with high-resolution time-of-flight aerosol mass spectrometry. *Environmental Science and Technology*, 42, 4478–4485. <https://doi.org/10.1021/es703009q>

AMAP. (2015). *AMAP Assessment 2015: Black carbon and ozone as Arctic climate forcers*. Oslo, Norway: Arctic Monitoring and Assessment Programme (AMAP). Retrieved from <http://www.amap.no/documents/doc/AMAP-Assessment-2015-Black-carbon-and-ozone-as-Arctic-climate-forcers/1299>

Barrie, L. A. (1986). Arctic air pollution: An overview of current knowledge. *Atmospheric Environment*, 20, 643–663. [https://doi.org/10.1016/0004-6981\(86\)90180-0](https://doi.org/10.1016/0004-6981(86)90180-0)

Bolton, D. (1980). The computation of equivalent potential temperature. *Monthly Weather Review*, 108, 1046–1053. [https://doi.org/10.1175/1520-0493\(1980\)108<1046:TCOEPT>2.0.CO;2](https://doi.org/10.1175/1520-0493(1980)108<1046:TCOEPT>2.0.CO;2)

Bond, T. C., Doherty, S. J., Fahey, D. W., Forster, P. M., Berntsen, T., DeAngelo, B. J., et al. (2013). Bounding the role of black carbon in the climate system: A scientific assessment. *Journal of Geophysical Research*, 118, 5380–5552. <https://doi.org/10.1002/jgrd.50171>

Browse, J., Carslaw, K. S., Arnold, S. R., Pringle, K., & Boucher, O. (2012). The scavenging processes controlling the seasonal cycle in the Arctic sulphate and black carbon aerosol. *Atmospheric Chemistry and Physics*, 12, 6775–6798. <https://doi.org/10.5194/acp-12-6775-2012>

Campbell, J. R., Hlavka, D. L., Spinhirne, J. D., Turner, D. D., & Flynn, C. J. (1998). Operational cloud boundary detection and analysis from micropulse lidar data. In Proc. 8th atmospheric radiation measurement (ARM) science team meeting (pp. 119–122). Tucson, AZ.

Campbell, J. R., Hlavka, D. L., Welton, E. J., Flynn, C. J., Turner, D. D., Spinhirne, J. D., et al. (2002). Full-time, eye-safe cloud and aerosol lidar observation at Atmospheric Radiation Measurement program sites: Instruments and data processing. *Journal of Atmospheric and Oceanic Technology*, 19, 431–442. [https://doi.org/10.1175/1520-0426\(2002\)019<0431:FTESCA>2.0.CO;2](https://doi.org/10.1175/1520-0426(2002)019<0431:FTESCA>2.0.CO;2)

Campbell, J. R., & Shiobara, M. (2008). Glaciation of a mixed-phase boundary layer cloud at a coastal arctic site as depicted in continuous lidar measurements. *Polar Science*, 2, 121–127. <https://doi.org/10.1016/j.polar.2008.04.004>

Cozic, J., Verheggen, B., Mertes, S., Connolly, P., Bower, K., Petzold, A., et al. (2007). Scavenging of black carbon in mixed phase clouds at the high alpine site Jungfraujoch. *Atmospheric Chemistry and Physics*, 7, 1797–1807. <https://doi.org/10.5194/acp-7-1797-2007>

Eleftheriadis, K., Vratolis, S., & Nyeki, S. (2009). Aerosol black carbon in the European Arctic: Measurements at Zeppelin station, Ny-Ålesund, Svalbard from 1998–2007. *Geophysical Research Letters*, 36, L02809. <https://doi.org/10.1029/2008GL035741>

Eyring, V., Bony, S., Meehl, G. A., Senior, C. A., Stevens, B., Stouffer, R. J., & Taylor, K. E. (2016). Overview of the Coupled Model Inter-comparison Project Phase 6 (CMIP6) experimental design and organization. *Geoscientific Model Development*, 9, 1937–1958. <https://doi.org/10.5194/gmd-9-1937-2016>

Førland, E. J., & Hanssen-Bauer, I. (2000). Increased precipitation in the Norwegian Arctic: True or false? *Climatic Change*, 46, 485–509. <https://doi.org/10.1023/A:1005613304674>

Førland, E. J., & Hanssen-Bauer, I. (2003). Past and future climate variations in the Norwegian Arctic: Overview and novel analyses. *Polar Research*, 22, 113–124. <https://doi.org/10.3402/polar.v22i2.6450>

Gierens, R., Kneifel, S., Shupe, M. D., Ebell, K., Maturilli, M., & Löhnert, U. (2020). Low-level mixed-phase clouds in a complex Arctic environment. *Atmospheric Chemistry and Physics*, 20, 3459–3481. <https://doi.org/10.5194/acp-20-3459-2020>

Hadley, O. L., & Kirchstetter, T. W. (2012). Black carbon reduction of snow albedo. *Nature Climate Change*, 2, 437–440. <https://doi.org/10.1038/nclimate1433>

Hanssen-Bauer, I., Førland, E. J., & Nordli, P. Ø. (1996). Measured and true precipitation at Svalbard. *Norwegian Meteorological Institute Report*, 31/96 KLIMA (p. 46).

Hawley, M. E., Galloway, J. N., & Keene, W. C. (1988). Standard error calculations for non-sea salt constituents in marine precipitation. *Water, Air, and Soil Pollution*, 42, 87–102. <https://doi.org/10.1007/bf00282393>

Hegg, D. A., Clarke, A. D., Doherty, S. J., & Ström, J. (2011). Measurements of black carbon aerosol washout ratio on Svalbard. *Tellus B*, 63, 891–900. <https://doi.org/10.1111/j.1600-0889.2011.00577.x>

Hirdman, D., Sodemann, H., Eckhardt, S., Burkhardt, J. F., Jefferson, A., Mefford, T., et al. (2010). Source identification of short-lived air pollutants in the Arctic using statistical analysis of measurement data and particle dispersion model output. *Atmospheric Chemistry and Physics*, 10, 669–693. <https://doi.org/10.5194/acp-10-669-2010>

Huang, L., Gong, S. L., Jia, C. Q., & Lavoue, D. (2010). Importance of deposition process in simulating the seasonality of the Arctic black carbon aerosol. *Journal of Geophysical Research*, 115, D17207. <https://doi.org/10.1029/2009JD013478>

Huang, L., Gong, S. L., Sharma, S., Lavoue, D., & Jia, C. Q. (2010). A trajectory analysis of atmospheric transport of black carbon aerosols to Canadian high Arctic in winter and spring (1990–2005). *Atmospheric Chemistry and Physics*, 10, 5065–5073. <https://doi.org/10.5194/acp-10-5065-2010>

- Jacobi, H.-W., Obleitner, F., Da Costa, S., Ginot, P., Eleftheriadis, K., Aas, W., & Zanutta, M. (2019). Deposition of ionic species and black carbon to the Arctic snowpack: Combining snow pit observations with modeling. *Atmospheric Chemistry and Physics*, *19*, 10361–10377. <https://doi.org/10.5194/acp-19-10361-2019>
- Jung, C. H., Yoon, Y. J., Kang, H. J., Gim, Y., Lee, B. Y., Ström, J., et al. (2018). The seasonal characteristics of cloud condensation nuclei (CCN) in the arctic lower troposphere. *Tellus B: Chemical and Physical Meteorology*, *70*, 1–13. <https://doi.org/10.1080/16000889.2018.1513291>
- Kaiser, J. W., Heil, A., Andreae, M. O., Benedetti, A., Chubarova, N., Jones, L., et al. (2012). Biomass burning emissions estimated with a Global Fire Assimilation System based on observed fire radiative power. *Biogeosciences*, *9*, 527–554. <https://doi.org/10.5194/bg-9-527-2012>
- Katich, J. M., Perring, A. E., & Schwarz, J. P. (2017). Optimized detection of particulates from liquid samples in the aerosol phase: Focus on black carbon. *Aerosol Science and Technology*, *51*, 543–553. <https://doi.org/10.1080/02786826.2017.1280597>
- Keene, W. C., Pszenny, A. A. P., Galloway, J. N., & Hawley, M. E. (1986). Sea-salt corrections and interpretation of constituent ratios in marine precipitation. *Journal of Geophysical Research*, *91*, 6647–6658. <https://doi.org/10.1029/JD091iD06p06647>
- Kinase, T., Adachi, K., Oshima, N., Goto-Azuma, K., Ogawa-Tsukagawa, Y., Kondo, Y., et al. (2020). Concentrations and size distributions of black carbon in the surface snow of eastern Antarctica in 2011. *Journal of Geophysical Research: Atmospheres*, *125*, e2019JD030737. <https://doi.org/10.1029/2019JD030737>
- Kodros, J. K., Hanna, S. J., Bertram, A. K., Leaitch, W. R., Schulz, H., Herber, A. B., et al. (2018). Size-resolved mixing state of black carbon in the Canadian high Arctic and implications for simulated direct radiative effect. *Atmospheric Chemistry and Physics*, *18*, 11345–11361. <https://doi.org/10.5194/acp-18-11345-2018>
- Koike, M., Goto-Azuma, K., Kondo, Y., Matsui, H., Mori, T., Moteki, N., et al. (2021). Studies on Arctic aerosols and clouds during the ArCS project. *Polar Science*, *27*, 100621. <https://doi.org/10.1016/j.polar.2020.100621>
- Koike, M., Ukita, J., Ström, J., Tunved, P., Shiobara, M., Vitale, V., et al. (2019). Year-round in situ measurements of Arctic low-level clouds: Microphysical properties and their relationships with aerosols. *Journal of Geophysical Research: Atmospheres*, *124*, 1798–1822. <https://doi.org/10.1029/2018JD029802>
- Kondo, Y. (2015). Effects of black carbon on climate: Advances in measurement and modeling. *Monographs on Environment, Earth and Planets*, *3*, 1–85. <https://doi.org/10.5047/meeep.2015.00301.0001>
- Kondo, Y., Matsui, H., Moteki, N., Sahu, L., Takegawa, N., Kajino, M., et al. (2011). Emissions of black carbon, organic, and inorganic aerosols from biomass burning in North America and Asia in 2008. *Journal of Geophysical Research*, *116*, D08204. <https://doi.org/10.1029/2010JD015152>
- Kondo, Y., Moteki, N., Oshima, N., Ohata, S., Koike, M., Shibano, Y., et al. (2016). Effects of wet deposition on the abundance and size distribution of black carbon in East Asia. *Journal of Geophysical Research: Atmospheres*, *121*, 4691–4712. <https://doi.org/10.1002/2015JD024479>
- Kondo, Y., Sahu, L., Kuwata, M., Miyazaki, Y., Takegawa, N., Moteki, N., et al. (2009). Stabilization of the mass absorption cross section of black carbon for filter-based absorption photometry by the use of a heated inlet. *Aerosol Science and Technology*, *43*, 741–756. <https://doi.org/10.1080/02786820902889879>
- Kondo, Y., Sahu, L., Moteki, N., Khan, F., Takegawa, N., Liu, X., et al. (2011). Consistency and traceability of black carbon measurements made by laser-induced incandescence, thermal-optical transmittance, and filter-based photo-absorption techniques. *Aerosol Science and Technology*, *45*, 295–312. <https://doi.org/10.1080/02786826.2010.533215>
- Konya, K., Yamaguchi, M., Takigawa, M., Miyakawa, T., & O'Neel, S. (2021). Mass concentration and origin of black carbon in spring snow on glaciers in the Alaska Range. *Polar Science*, *27*, 100572. <https://doi.org/10.1016/j.polar.2020.100572>
- Kuwata, M., Zorn, S. R., & Martin, S. T. (2012). Using elemental ratios to predict the density of organic material composed of carbon, hydrogen, and oxygen. *Environmental Science and Technology*, *46*, 787–794. <https://doi.org/10.1021/es202525q>
- Lamarque, J.-F., Bond, T. C., Eyring, V., Granier, C., Heil, A., Klimont, Z., et al. (2010). Historical (1850–2000) gridded anthropogenic and biomass burning emissions of reactive gases and aerosols: Methodology and application. *Atmospheric Chemistry and Physics*, *10*, 7017–7039. <https://doi.org/10.5194/acp-10-7017-2010>
- Latham, T. L., Beyersdorf, A. J., Thornhill, K. L., Winstead, E. L., Cubison, M. J., Hecobian, A., et al. (2013). Analysis of CCN activity of Arctic aerosol and Canadian biomass burning during summer 2008. *Atmospheric Chemistry and Physics*, *13*, 2735–2756. <https://doi.org/10.5194/acp-13-2735-2013>
- Leaitch, W. R., Korolev, A., Aliabadi, A. A., Burkart, J., Willis, M. D., Abbatt, J. P. D., et al. (2016). Effects of 20–100 nm particles on liquid clouds in the clean summertime Arctic. *Atmospheric Chemistry and Physics*, *16*, 11107–11124. <https://doi.org/10.5194/acp-16-11107-2016>
- Liu, D., Quennehen, B., Darbyshire, E., Allan, J. D., Williams, P. I., Taylor, J. W., et al. (2015). The importance of Asia as a source of black carbon to the European Arctic during springtime 2013. *Atmospheric Chemistry and Physics*, *15*, 11537–11555. <https://doi.org/10.5194/acp-15-11537-2015>
- Macdonald, K. M., Sharma, S., Toom, D., Chivulescu, A., Hanna, S., Bertram, A. K., et al. (2017). Observations of atmospheric chemical deposition to high Arctic snow. *Atmospheric Chemistry and Physics*, *17*, 5775–5788. <https://doi.org/10.5194/acp-17-5775-2017>
- Mahmood, R., von Salzen, K., Flanner, M., Sand, M., Langner, J., Wang, H., & Huang, L. (2016). Seasonality of global and Arctic black carbon processes in the Arctic Monitoring and Assessment Programme models. *Journal of Geophysical Research: Atmospheres*, *121*, 7100–7116. <https://doi.org/10.1002/2016JD024849>
- Marquette, L., Kaspari, S., & Simões, J. C. (2020). Mass and number size distributions of rBC in snow and firn samples from Pine Island Glacier, West Antarctica. *Earth and Space Science*, *7*, e2020EA001198. <https://doi.org/10.1029/2020EA001198>
- Matsui, H., Hamilton, D. S., & Mahowald, N. M. (2018). Black carbon radiative effects highly sensitive to emitted particle size when resolving mixing-state diversity. *Nature Communications*, *9*, 3446. <https://doi.org/10.1038/s41467-018-05635-1>
- Matsui, H., & Moteki, N. (2020). High sensitivity of Arctic black carbon radiative effects to subgrid vertical velocity in aerosol activation. *Geophysical Research Letters*, *47*, e2020GL088978. <https://doi.org/10.1029/2020GL088978>
- Maturilli, M., & Ebell, K. (2018). Twenty-five years of cloud base height measurements by ceilometer in Ny-Ålesund. *Earth System Science Data*, *10*, 1451–1456. <https://doi.org/10.5194/essd-10-1451-2018>
- Maturilli, M., & Kayser, M. (2017). Arctic warming, moisture increase and circulation changes observed in the Ny-Ålesund homogenized radiosonde record. *Theoretical and Applied Climatology*, *130*, 1–17. <https://doi.org/10.1007/s00704-016-1864-0>
- Mori, T. (2017). *Observational studies on wet deposition mechanism of black carbon particles*. Tokyo, Japan: The University of Tokyo. <https://doi.org/10.15083/00075627>
- Mori, T., Goto-Azuma, K., Kondo, Y., Ogawa-Tsukagawa, Y., Miura, K., Hirabayashi, M., et al. (2019). Black carbon and inorganic aerosols in Arctic snowpack. *Journal of Geophysical Research: Atmospheres*, *124*, 13325–13356. <https://doi.org/10.1029/2019JD030623>

- Mori, T., Kondo, Y., Ohata, S., Moteki, N., Matsui, H., Oshima, N., & Iwasaki, A. (2014). Wet deposition of black carbon at a remote site in the East China Sea. *Journal of Geophysical Research: Atmospheres*, *119*, 10485–10498. <https://doi.org/10.1002/2014JD022103>
- Mori, T., Kondo, Y., Ohata, S., Zhao, Y., Sinha, P. R., Oshima, N., et al. (2020). Seasonal variation of wet deposition of black carbon in Arctic Alaska. *Journal of Geophysical Research: Atmospheres*, *125*, e2019JD032240. <https://doi.org/10.1029/2019JD032240>
- Mori, T., Moteki, N., Ohata, S., Koike, M., Goto-Azuma, K., Miyazaki, Y., & Kondo, Y. (2016). Improved technique for measuring the size distribution of black carbon particles in liquid water. *Aerosol Science and Technology*, *50*(3), 242–254. <https://doi.org/10.1080/02786826.2016.1147644>
- Moteki, N., & Kondo, Y. (2010). Dependence of laser-induced incandescence on physical properties of black carbon aerosols: Measurements and theoretical interpretation. *Aerosol Science and Technology*, *44*, 663–675. <https://doi.org/10.1080/02786826.2010.484450>
- Moteki, N., Kondo, Y., Oshima, N., Takegawa, N., Koike, M., Kita, K., et al. (2012). Size dependence of wet removal of black carbon aerosols during transport from the boundary layer to the free troposphere. *Geophysical Research Letters*, *39*, L13802. <https://doi.org/10.1029/2012GL052034>
- Moteki, N., & Mori, T. (2015). Theoretical analysis of a method to measure size distributions of solid particles in water by aerosolization. *Journal of Aerosol Science*, *83*, 25–31. <https://doi.org/10.1016/j.jaerosci.2015.02.002>
- Moteki, N., Mori, T., Matsui, H., & Ohata, S. (2019). Observational constraint of in-cloud supersaturation for simulations of aerosol rainout in atmospheric models. *npj Climate and Atmospheric Science*, *2*. <https://doi.org/10.1038/s41612-019-0063-y>
- Motos, G., Schmale, J., Corbin, J. C., Modini, R. L., Karlen, N., Bertö, M., et al. (2019). Cloud droplet activation properties and scavenged fraction of black carbon in liquid-phase clouds at the high-alpine research station Jungfraujoch (3580 m a.s.l.). *Atmospheric Chemistry and Physics*, *19*, 3833–3855. <https://doi.org/10.5194/acp-19-3833-2019>
- Murphy, D. M., & Koop, T. (2005). Review of the vapour pressures of ice and supercooled water for atmospheric applications. *Quarterly Journal of the Royal Meteorological Society*, *131*, 1539–1565. <https://doi.org/10.1256/qj.04.94>
- Nomokonova, T., Ebell, K., Löhnert, U., Maturilli, M., Ritter, C., & O'Connor, E. (2019). Statistics on clouds and their relation to thermodynamic conditions at Ny-Ålesund using ground-based sensor synergy. *Atmospheric Chemistry and Physics*, *19*, 4105–4126. <https://doi.org/10.5194/acp-19-4105-2019>
- Ohata, S., Kondo, Y., Moteki, N., Mori, T., Yoshida, A., Sinha, P. R., & Koike, M. (2019). Accuracy of black carbon measurements by a filter-based absorption photometer with a heated inlet. *Aerosol Science and Technology*, *53*, 1079–1091. <https://doi.org/10.1080/02786826.2019.1627283>
- Ohata, S., Moteki, N., Mori, T., Koike, M., & Kondo, Y. (2016). A key process controlling the wet removal of aerosols: New observational evidence. *Scientific Reports*, *6*, 34113. <https://doi.org/10.1038/srep34113>
- Ohata, S., Schwarz, J. P., Moteki, N., Koike, M., Takami, A., & Kondo, Y. (2016). Hygroscopicity of materials internally mixed with black carbon measured in Tokyo. *Journal of Geophysical Research: Atmospheres*, *121*, 362–381. <https://doi.org/10.1002/2015JD024153>
- Oshima, N., Yukimoto, S., Deushi, M., Koshiro, T., Kawai, H., Tanaka, T. Y., & Yoshida, K. (2020). Global and Arctic effective radiative forcing of anthropogenic gases and aerosols in MRI-ESM2.0. *Progress in Earth and Planetary Science*, *7*, 38. <https://doi.org/10.1186/s40645-020-00348-w>
- Peters, M. D., & Kreidenweis, S. M. (2007). A single parameter representation of hygroscopic growth and cloud condensation nucleus activity. *Atmospheric Chemistry and Physics*, *7*, 1961–1971. <https://doi.org/10.5194/acp-7-1961-2007>
- Qi, L., Li, Q., He, C., Wang, X., & Huang, J. (2017). Effects of Wegener-Bergeron-Findeisen process on global black carbon distribution. *Atmospheric Chemistry and Physics*, *17*, 7459–7479. <https://doi.org/10.5194/acp-17-7459-2017>
- Quinn, P. K., Shaw, G., Andrews, E., Dutton, E. G., Ruoho-Airola, T., & Gong, S. L. (2007). Arctic haze: Current trends and knowledge gaps. *Tellus B*, *59*, 99–114. <https://doi.org/10.1111/j.1600-0889.2006.00236.x>
- Rasmussen, R., Baker, B., Kochendorfer, J., Meyers, T., Landolt, S., Fischer, A. P., et al. (2012). How well are we measuring snow: The NOAA/FAA/NCAR winter precipitation test bed. *Bulletin of the American Meteorological Society*, *93*, 811–829. <https://doi.org/10.1175/BAMS-D-11-00052.1>
- Rinke, A., Maturilli, M., Graham, R. M., Matthes, H., Handorf, D., Cohen, L., et al. (2017). Extreme cyclone events in the Arctic: Wintertime variability and trends. *Environmental Research Letters*, *12*, 094006. <https://doi.org/10.1088/1748-9326/aa7def>
- Russell, L. M. (2003). Aerosol organic-mass-to-organic-carbon ratio measurements. *Environmental Science and Technology*, *37*, 2982–2987. <https://doi.org/10.1021/es026123w>
- Schmale, J., Arnold, S. R., Law, K. S., Thorp, T., Anenber, S., Simpson, W. R., et al. (2018). Local Arctic air pollution: A neglected but serious problem. *Earth's Future*, *6*, 1385–1412. <https://doi.org/10.1029/2018EF000952>
- Schroder, J. C., Hanna, S. J., Modini, R. L., Corrigan, A. L., Kreidenweis, S. M., Macdonald, A. M., et al. (2015). Size-resolved observations of refractory black carbon particles in cloud droplets at a marine boundary layer site. *Atmospheric Chemistry and Physics*, *15*, 1367–1383. <https://doi.org/10.5194/acp-15-1367-2015>
- Schulz, H., Bozem, H., Zanatta, M., Leitch, W. R., Herber, A. B., Burkart, J., et al. (2019). High-Arctic aircraft measurements characterizing black carbon vertical variability in spring and summer. *Atmospheric Chemistry and Physics*, *19*, 2361–2384. <https://doi.org/10.5194/acp-19-2361-2019>
- Schwarz, J. P., Gao, R. S., Spackman, J. R., Watts, L. A., Thomson, D. S., Fahey, D. W., et al. (2008). Measurement of the mixing state, mass, and optical size of individual black carbon particles in urban and biomass burning emissions. *Geophysical Research Letters*, *35*, L13810. <https://doi.org/10.1029/2007JD009042>
- Schwarz, J. P., Spackman, J. R., Gao, R. S., Perring, A. E., Cross, E., Onasch, T. B., et al. (2010). The detection efficiency of the single particle soot photometer. *Aerosol Science and Technology*, *44*, 612–628. <https://doi.org/10.1080/02786826.2010.481298>
- Seinfeld, J. H., & Pandis, S. N. (2016). *Atmospheric chemistry and physics: From air pollution to climate change*. Hoboken, NJ: John Wiley & Sons.
- Serreze, M. C., & Barrett, A. P. (2008). The summer cyclone maximum over the Central Arctic Ocean. *Journal of Climate*, *21*, 1048–1065. <https://doi.org/10.1175/2007JCLI1810.1>
- Sharma, S., Andrews, E., Barrie, L. A., Ogren, J. A., & Lavoué, D. (2006). Variations and sources of the equivalent black carbon in the high Arctic revealed by long-term observations at Alert and Barrow: 1989–2003. *Journal of Geophysical Research*, *111*, D14208. <https://doi.org/10.1029/2005JD006581>
- Sharma, S., Ishizawa, M., Chan, D., Lavoué, D., Andrews, E., Eleftheriadis, K., & Maksyutov, S. (2013). 16-year simulation of Arctic black carbon: Transport, source contribution, and sensitivity analysis on deposition. *Journal of Geophysical Research*, *118*, 943–964. <https://doi.org/10.1029/2012JD017774>
- Shen, Z., Ming, Y., Horowitz, L. W., Ramaswamy, V., & Lin, M. (2017). On the seasonality of Arctic black carbon. *Journal of Climate*, *30*, 4429–4441. <https://doi.org/10.1175/JCLI-D-16-0580.1>

- Shibata, T., Shiraiishi, K., Shiobara, M., Iwasaki, S., & Takano, T. (2018). Seasonal variations in high Arctic free tropospheric aerosols over Ny-Ålesund, Svalbard, observed by ground-based lidar. *Journal of Geophysical Research: Atmospheres*, *123*, 12353–12367. <https://doi.org/10.1029/2018JD028973>
- Shiobara, M., Yabuki, M., & Kobayasi, H. (2003). A polar cloud analysis based on micropulse lidar measurements at Ny-Alesund, Svalbard and Syowa, Antarctica. *Physics and Chemistry of the Earth*, *28*(28), 1205–1212. <https://doi.org/10.1016/j.pce.2003.08.057>
- Shiraiwa, M., Kondo, Y., Moteki, N., Takegawa, N., Sahu, L. K., Takami, A., et al. (2008). Radiative impact of mixing state of black carbon aerosol in Asian outflow. *Journal of Geophysical Research*, *113*, D24210. <https://doi.org/10.1029/2008JD010546>
- Shupe, M. D. (2011). Clouds at Arctic atmospheric observatories. Part II: Thermodynamic phase characteristics. *Journal of Applied Meteorology and Climatology*, *50*, 645–661. <https://doi.org/10.1175/2010JAMC2468.1>
- Sinha, P. R., Kondo, Y., Goto-Azuma, K., Tsukagawa, Y., Fukuda, K., Koike, M., et al. (2018). Seasonal progression of the deposition of black carbon by snowfall at Ny-Ålesund, Spitsbergen. *Journal of Geophysical Research: Atmospheres*, *123*, 997–1016. <https://doi.org/10.1002/2017JD028027>
- Sinha, P. R., Kondo, Y., Koike, M., Ogren, J. A., Jefferson, A., Barrett, T. E., et al. (2017). Evaluation of ground-based black carbon measurements by filter-based photometers at two Arctic sites. *Journal of Geophysical Research: Atmospheres*, *122*, 3544–3572. <https://doi.org/10.1002/2016JD025843>
- Straka, J. M. (2009). *Cloud and precipitation microphysics: Principles and parameterizations*. Cambridge University Press.
- Wang, X., Shi, T., Zhang, X., & Chen, Y. (2020). An overview of snow albedo sensitivity to black carbon contamination and snow grain properties based on experimental datasets across the Northern Hemisphere. *Current Pollution Reports*, *6*, 368–379. <https://doi.org/10.1007/s40726-020-00157-1>
- Wang, X., Zhang, L., & Moran, M. (2010). Uncertainty assessment of current size-resolved parameterizations for below-cloud particle scavenging by rain. *Atmospheric Chemistry and Physics*, *10*, 5685–5705. <https://doi.org/10.5194/acp-10-5685-2010>
- Willis, M. D., Leaitch, W. R., & Abbatt, J. P. (2018). Processes controlling the composition and abundance of Arctic aerosol. *Reviews of Geophysics*, *56*, 621–671. <https://doi.org/10.1029/2018RG000602>
- Yeo, H., Park, S.-J., Kim, B.-M., Shiobara, M., Kim, S.-W., Kwon, H., et al. (2018). The observed relationship of cloud to surface longwave radiation and air temperature at Ny-Ålesund, Svalbard. *Tellus B*, *70*, 1–10. <https://doi.org/10.1080/16000889.2018.1450589>
- Yoshida, A., Moteki, N., Ohata, S., Mori, T., Koike, M., Kondo, K., et al. (2020). Abundances and microphysical properties of light-absorbing iron oxide and black carbon aerosols over East Asia and the Arctic. *Journal of Geophysical Research: Atmospheres*, *125*, e2019JD032301. <https://doi.org/10.1029/2019JD032301>
- Zanatta, M., Laj, P., Gysel, M., Baltensperger, U., Vratolis, S., Eleftheriadis, K., et al. (2018). Effects of mixing state on optical and radiative properties of black carbon in the European Arctic. *Atmospheric Chemistry and Physics*, *18*, 14037–14057. <https://doi.org/10.5194/acp-18-14037-2018>
- Zhang, L., Wang, X., Moran, M. D., & Feng, J. (2013). Review and uncertainty assessment of size-resolved scavenging coefficient formulations for below-cloud snow scavenging of atmospheric aerosols. *Atmospheric Chemistry and Physics*, *13*, 10005–10025. <https://doi.org/10.5194/acp-13-10005-2013>
- Zhang, X. D., Walsh, J. E., Zhang, J., Bhatt, U. S., & Ikeda, M. (2004). Climatology and interannual variability of Arctic cyclone activity: 1948–2002. *Journal of Climate*, *17*, 2300–2317. [https://doi.org/10.1175/1520-0442\(2004\)017<2300:CAIVOA>2.0.CO;2](https://doi.org/10.1175/1520-0442(2004)017<2300:CAIVOA>2.0.CO;2)